The University Of Sheffield.

This is a repository copy of *Emissive spin-0 triplet-pairs are a direct product of triplet–triplet annihilation in pentacene single crystals and anthradithiophene films*.

Article:

Bossanyi, D.G. orcid.org/0000-0002-8804-802X, Matthiesen, M., Wang, S. et al. (9 more authors) (2021) Emissive spin-0 triplet-pairs are a direct product of triplet–triplet annihilation in pentacene single crystals and anthradithiophene films. Nature Chemistry, 13 (2). pp. 163-171. ISSN 1755-4330

https://doi.org/10.1038/s41557-020-00593-y

This is a post-peer-review, pre-copyedit version of an article published in Nature Chemistry. The final authenticated version is available online at: http://dx.doi.org/10.1038/s41557-020-00593-y.

Supplementary Information

Emissive spin-0 triplet-pairs are a direct product of triplet-triplet annihilation in pentacene single crystals and anthradithiophene films.

David G. Bossanyi[1,*], Maik Matthiesen[2], Shuangqing Wang[1], Joel A. Smith[1], Rachel C. Kilbride[1], James D. Shipp[3], Dimitri Chekulaev[3], Emma Holland[4], John E. Anthony[4], Jana Zaumseil[2], Andrew J. Musser[1,5], and Jenny Clark[1,*]

[1]Department of Physics and Astronomy, The University of Sheffield, Sheffield, UK
[2]Institute for Physical Chemistry, Heidelberg University, Heidelberg, Germany
[3]Department of Chemistry, The University of Sheffield, Sheffield, UK
[4]Department of Chemistry, University of Kentucky, Lexington, KY, USA
[5]Department of Chemistry and Chemical Biology, Cornell University, Ithaca, NY, USA

*Correspondence to: jenny.clark@sheffield.ac.uk

Contents

1 Sample preparation and characterisation

1.1 diftes thin film characterisation

Thin film preparation protocols and details of the GIWAXS and AFM measurements are provided in the Methods.

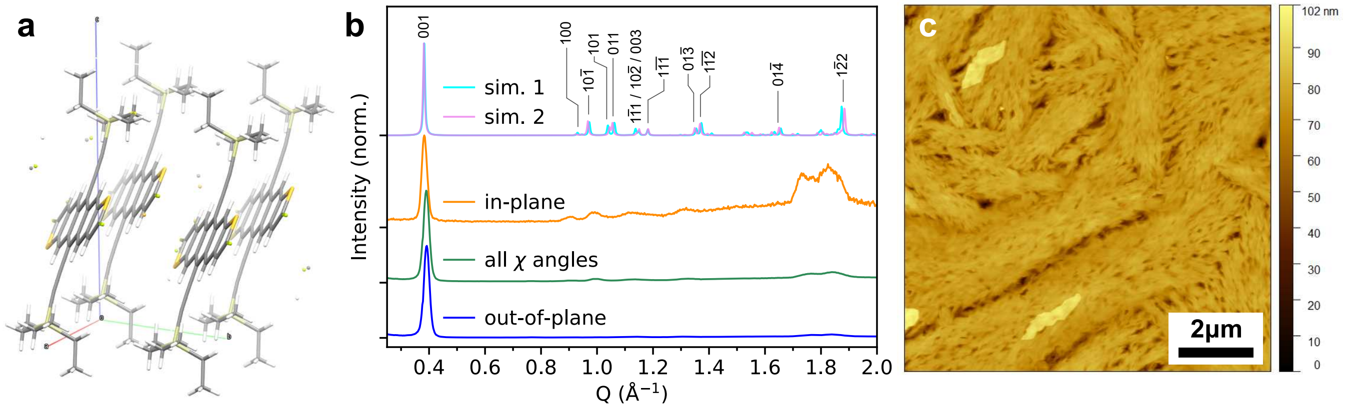

Figure 1 | Characterisation of diftes thin film. a, Crystal structure[1] of diftes, showing the brickwork packing. **b**, Simulated and experimental diffraction patterns for diftes. GIWAXS data was integrated through various χ angles normal to the beam incidence at the detector; out-of-plane (in the Q_z direction, $\chi = 90° \pm 20°$), in-plane (which includes all other angles, $0° \leq \chi \leq 70°$), and the full χ range. The out-of-plane scatter is dominated by a feature corresponding to the (001) plane, indicating a predominantly lamellar textured film (edge-on motif[2]). Simulated patterns were generated from Ref. 3 (light blue line, sim. 1) and Ref. 1 (purple line, sim. 2) with the latter acquired from a single crystal of the pure anti diftes isomer at 180 K. Slight peak shifts between the measured and simulated data could be explained by thermal expansion and modified crystal packing at room temperature. **c**, AFM scan of the film surface showing micron-scale crystalline texture similar to previous reports of diftes crystal growth with the edge-on motif[2].

1.2 Pentacene single crystal growth

A detailed description of the two-stage physical vapour transport growth process and subsequent crystal characterisation is given in the Methods.

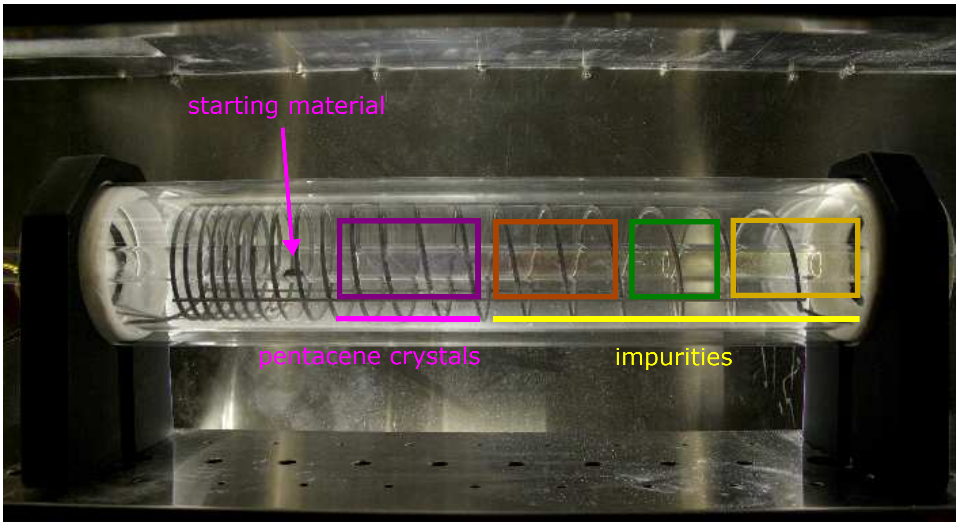

Figure 2 | Photograph of the PVT furnace taken during the first sublimation of pentacene. Purple pentacene crystals were observed in the leftmost (hottest) part of the crystallization zone, with orange, green and yellow impurities in the cooler regions.

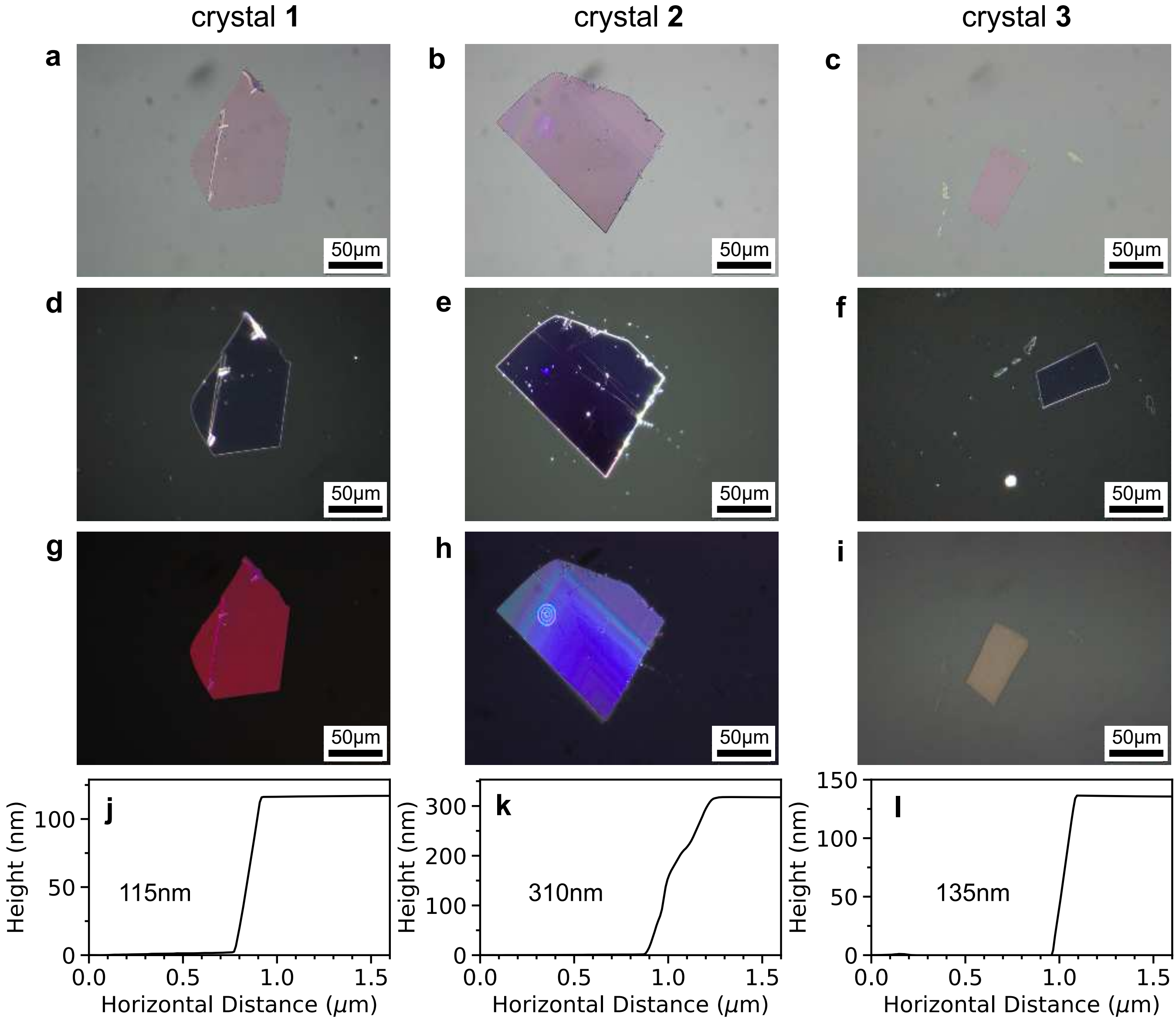

Figure 3 | Pentacene single crystal characterisation. **a-i**, Microscope images of pentacene single crystals **1-3**. Bright-field **a-c**, dark-field **d-f** and cross-polarised **g-i**. **j-l**, AFM measured thicknesses of the single crystals.

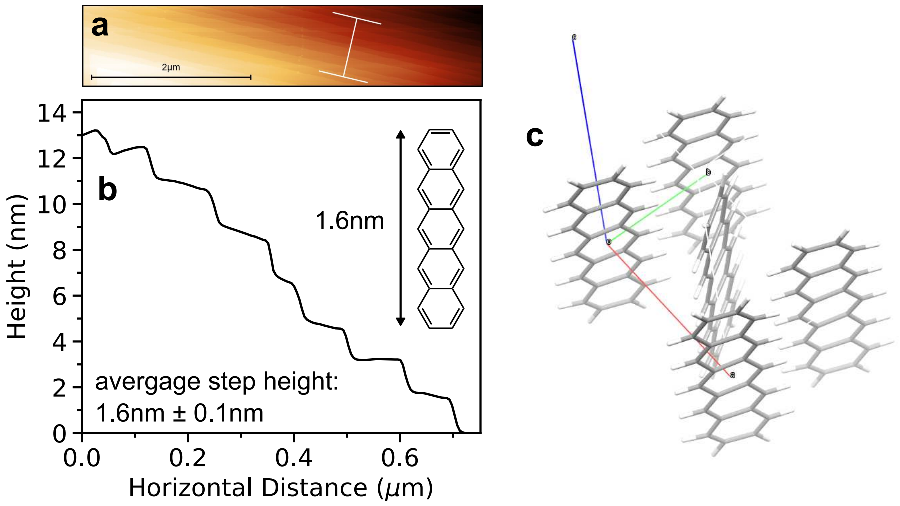

Figure 4 | Terraces on the surface of pentacene single crystal 2. **a**, AFM scan of the surface of pentacene single crystal **2**. The scale bar is 2 µm. **b**, Height profile of the surface, showing terraces of average step height 1.6 nm, corresponding to the c-axis of the pentacene crystal. **c**, Crystal structure of pentacene[4], showing the herringbone packing in the a-b plane.

2 Spectral sensitivity of the intensified CCD

Full details of the time-resolved PL measurements and data processing steps can be found in the Methods.

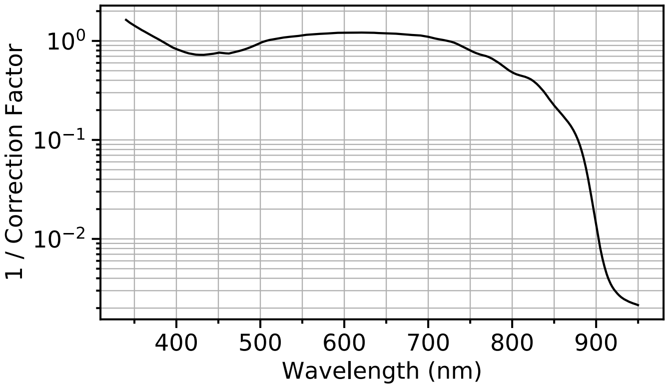

Figure 5 | Spectral sensitivity of the iCCD. diftes PL spectra are almost unaffected by the spectral sensitivity, which is roughly constant in the visible region. However, the emission from the pentacene single crystals in the NIR is substantially affected. All spectra have been corrected for spectral sensitivity.

3 Steady-state optical properties of diftes thin films

Figure 6 gives a summary of the temperature-dependent steady-state optical properties of the diftes thin film. The slight changes to the absorption spectrum (small redshift of S_1 and linewidth narrowing with decreasing temperature) are consistent with those seen in molecular crystals with some J-aggregate character[5]. The spectrum evolves smoothly: there is no obvious phase transition, consistent with previously reported temperature-dependent X-ray diffraction[6]. The photoluminescence demonstrates the increasing brightness of ^{1}(TT) emission with decreasing temperature, as well as the reduction in singlet contribution. We note the growth of a shoulder to the ^{1}(TT) emission spectrum for temperatures below 100 K: this has been observed previously[6] and likely arises from a redshifted, superradiant S_1.

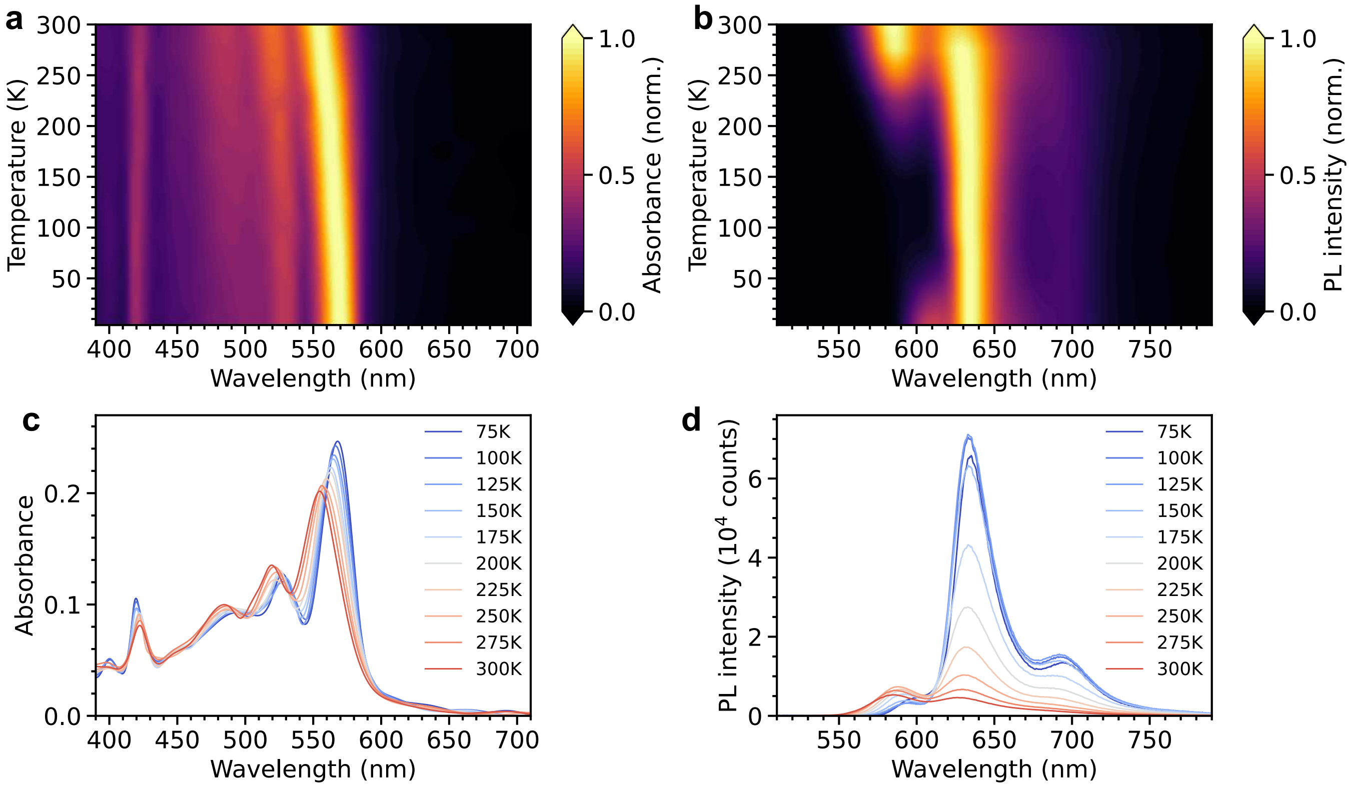

Figure 6 | Temperature dependence of diftes absorbance and PL. a, 2D map of the normalised ground state absorption spectrum. **b**, 2D map of the normalised steady-state PL. **c**, Temperature-dependent absorbance of the thin film sample. No significant changes with temperature are observed. **d**, Temperature-dependent steady-state PL of the thin film, showing the growth of the ^{1}(TT) emission at low temperature.

4 Extraction of ^{1}(TT) populations from diftes TRPL data

The extraction of spectral components was achieved using Multivariate Curve Resolution Alternating Least Squares (MCR-ALS)[7]. Details of the implementation are given in the Methods.

In general, the separation of S_1 and ^{1}(TT) components is only relevant during the first few nanoseconds, where singlet fission is 'smeared out' in our instrument response. Beyond a few nanoseconds, the spectrum does not change with time, and consists only of ^{1}(TT) at low temperatures or a mixture of ^{1}(TT) and S_1 at higher temperatures, which are anyway in equilibrium. Thus after the first few nanoseconds, the extracted dynamics are essentially identical to the wavelength-integrated PL.

At 200 K (Figure 10), the algorithm very successfully separated the ^{1}(TT) and S_1 spectra and we can see the equilibrium maintained between the two populations. However, at 250 K and 291 K, the algorithm did an imperfect job of fully separating the spectra; this is because the S_1 contribution starts to dominate leading to very little spectral change at all with time, even over the first few nanoseconds.

Despite the presence of a third component, the excimer, at an exciton density of 10^{17}cm^{-3} at 250 K, the MCR-ALS algorithm could not successfully extract it. This makes very little difference to the extracted dynamics, however (see the first point, above). The excimer was only observed at this particular temperature and low excitation density and over a limited timerange so we do not include it in the kinetic scheme (see Section 8 for more detail).

Figures 7-12 show 2D maps of the TRPL data (left column), extracted spectra (central column) and extracted population dynamics (right hand column) at temperatures of 77 K, 100 K, 150 K, 200 K, 250 K and 291 K.

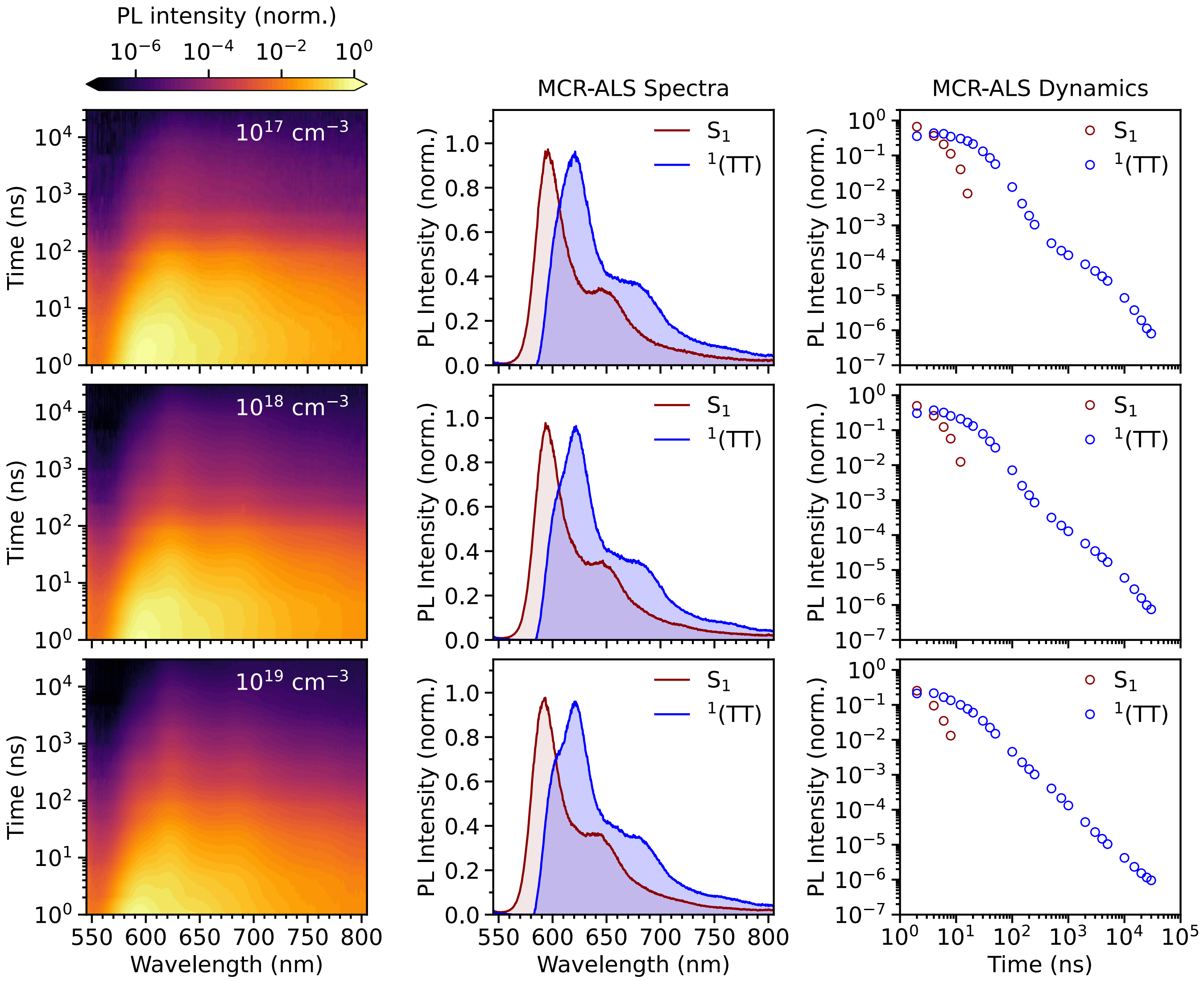

Figure 7 | Extraction of S_1 and ^{1}(TT) components by MCR-ALS at 77 K. 2D maps of the normalised TRPL data are shown in the left column, extracted spectra in the central column and extracted dynamics, normalised at 4 ns, in the right column. Initial exciton density varies from $10^{17}\mathrm{cm}^{-3}$ (top row) through $10^{18}\mathrm{cm}^{-3}$ (middle row) to $10^{19}\mathrm{cm}^{-3}$ (bottom row).

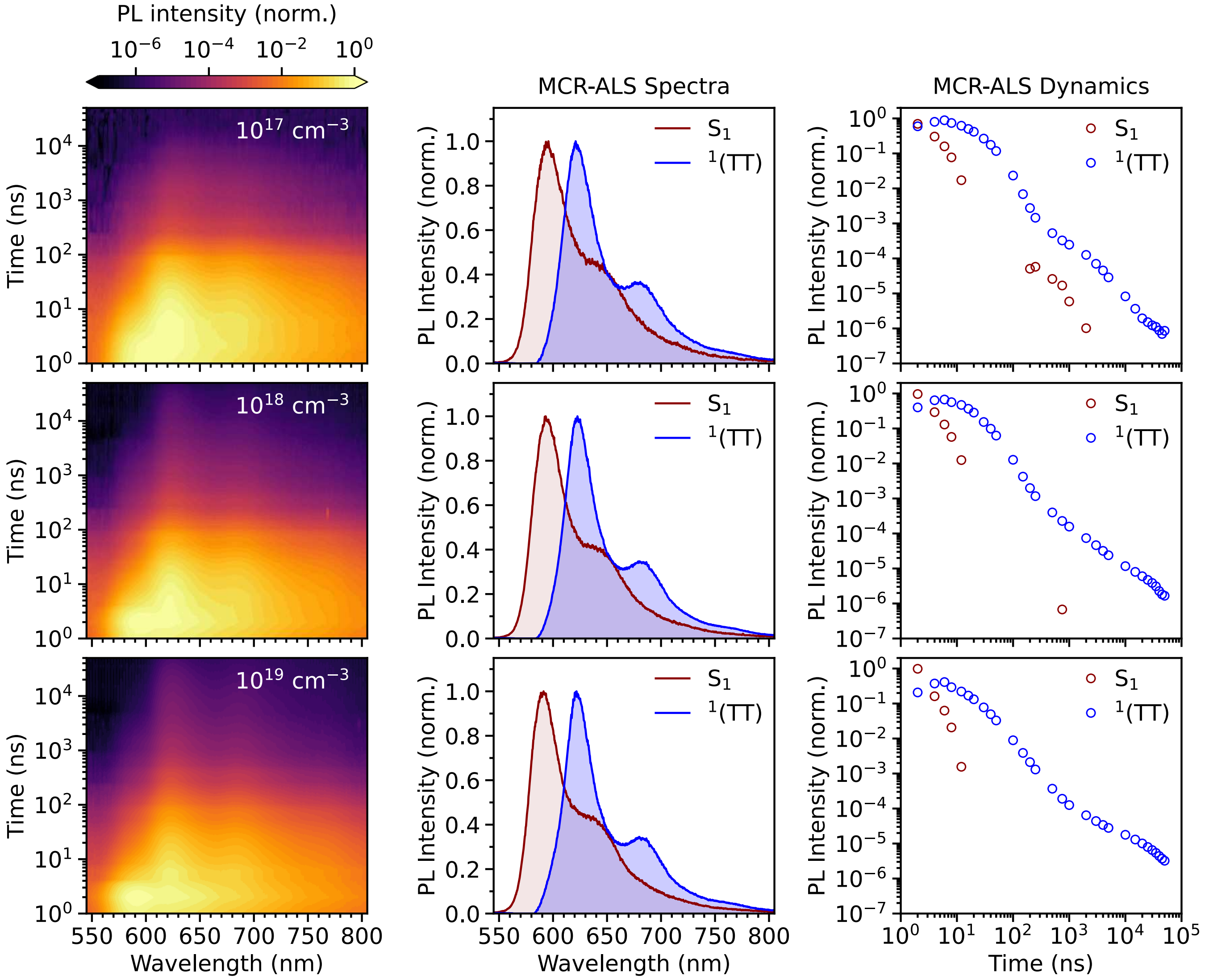

Figure 8 | **Extraction of S_1 and ^{1}(TT) components by MCR-ALS at 100 K.** 2D maps of the normalised TRPL data are shown in the left column, extracted spectra in the central column and extracted dynamics, normalised at 4 ns, in the right column. Initial exciton density varies from 10^{17}cm^{-3} (top row) through 10^{18}cm^{-3} (middle row) to 10^{19}cm^{-3} (bottom row).

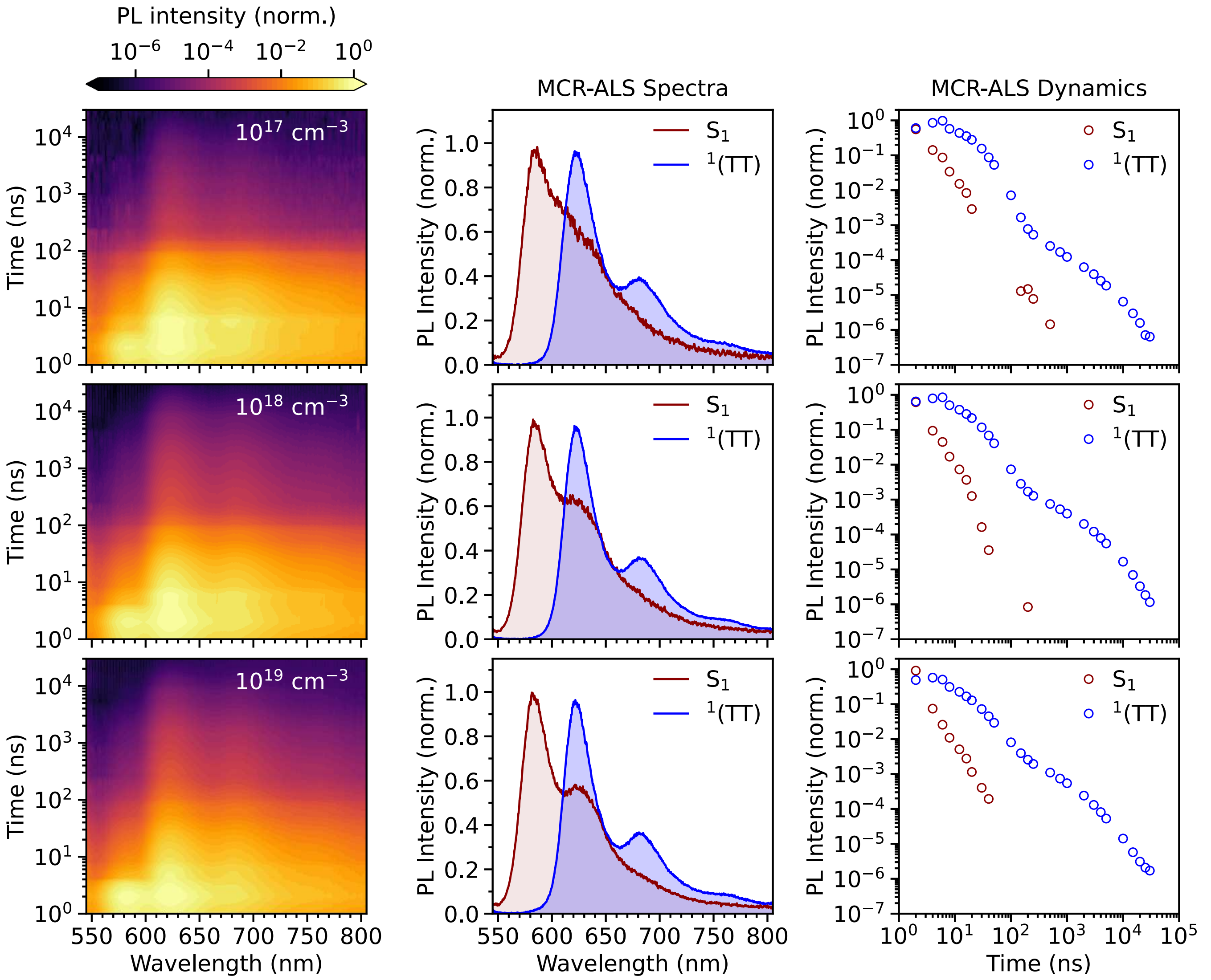

Figure 9 | Extraction of S_1 and ^{1}(TT) components by MCR-ALS at 150 K. 2D maps of the normalised TRPL data are shown in the left column, extracted spectra in the central column and extracted dynamics, normalised at 4 ns, in the right column. Initial exciton density varies from 10^{17}cm^{-3} (top row) through 10^{18}cm^{-3} (middle row) to 10^{19}cm^{-3} (bottom row).

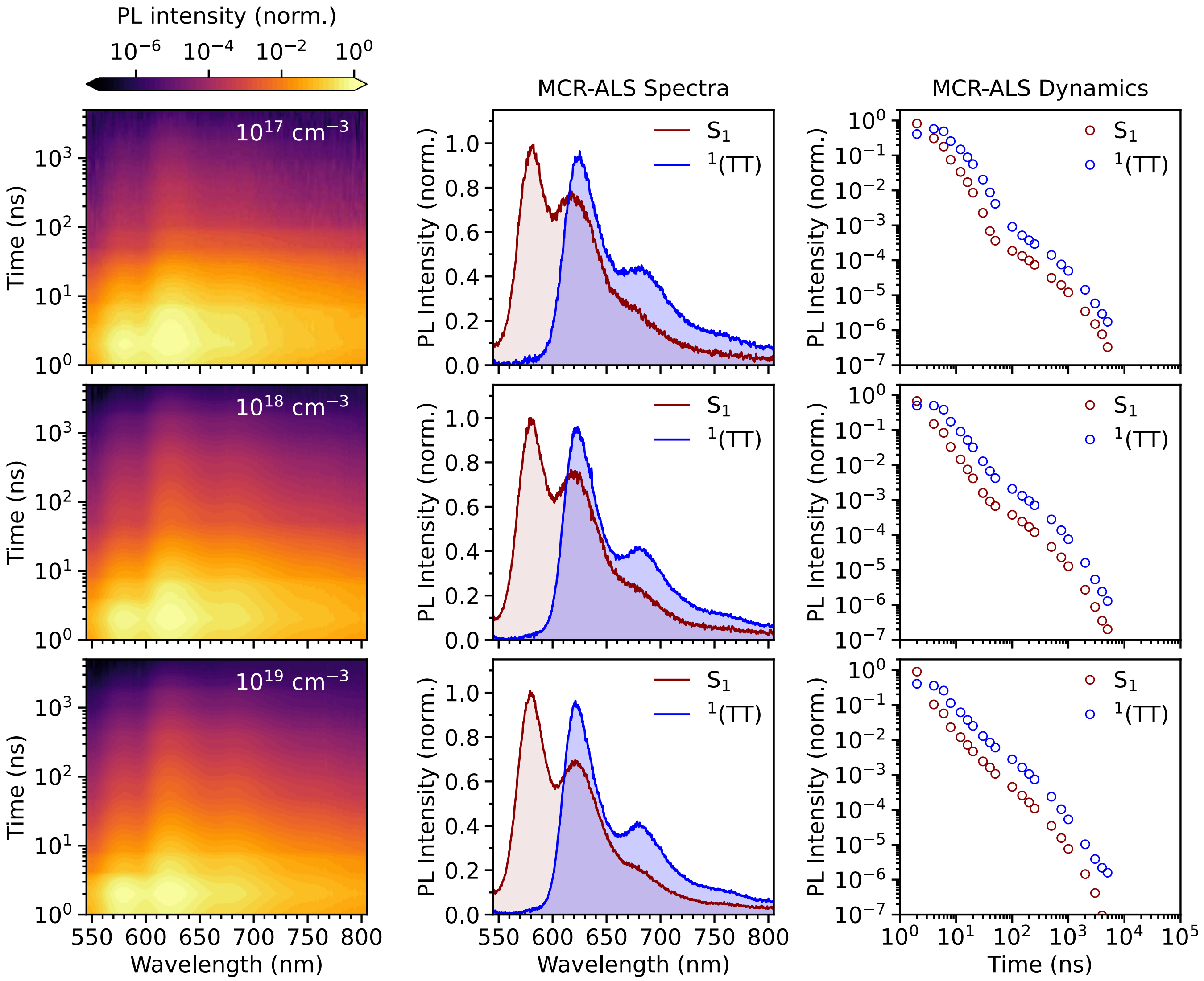

Figure 10 | Extraction of S_1 and ^{1}(TT) components by MCR-ALS at 200 K. 2D maps of the normalised TRPL data are shown in the left column, extracted spectra in the central column and extracted dynamics, normalised at 4 ns, in the right column. Initial exciton density varies from 10^{17}cm^{-3} (top row) through 10^{18}cm^{-3} (middle row) to 10^{19}cm^{-3} (bottom row).

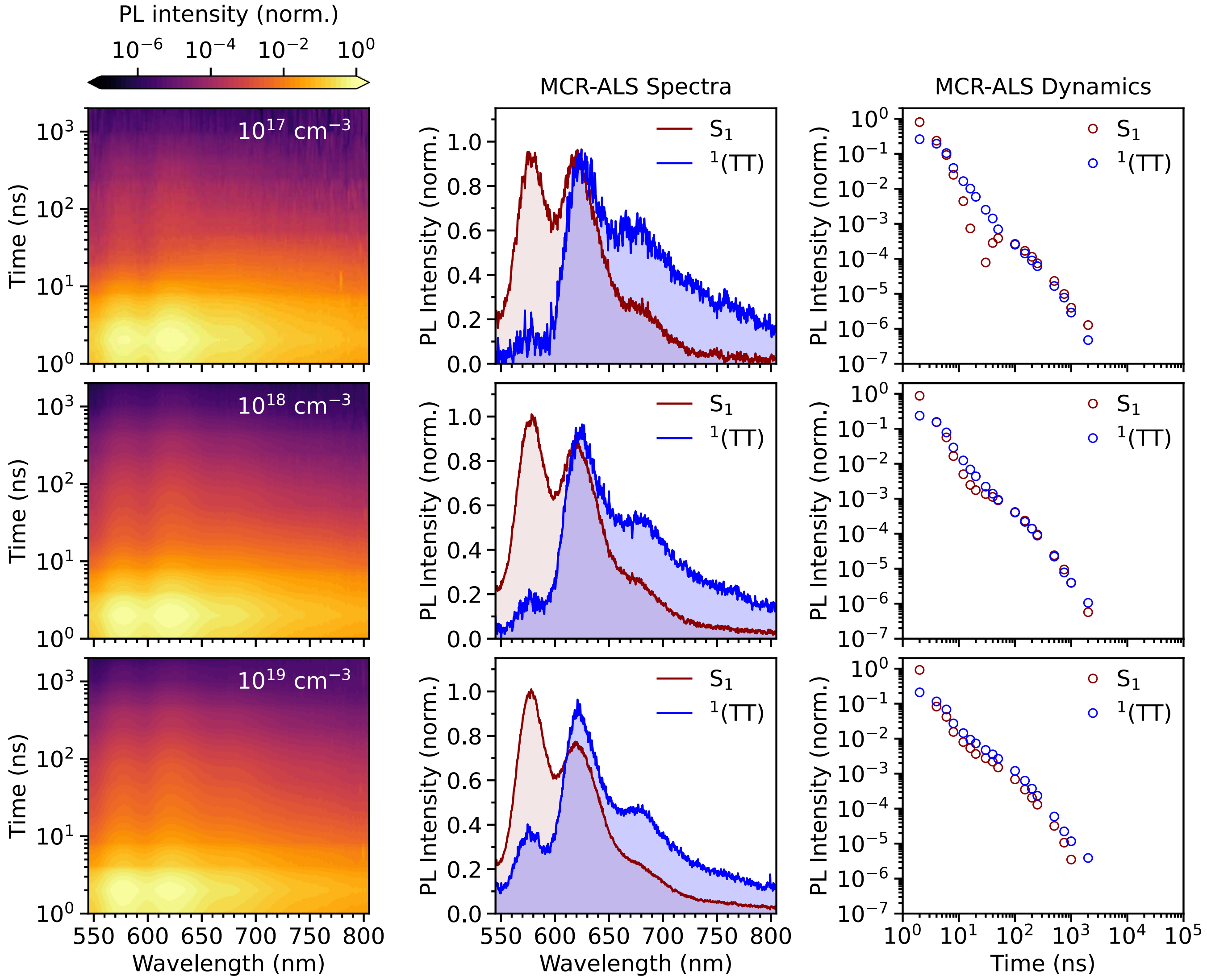

Figure 11 | Extraction of S_1 and ^{1}(TT) components by MCR-ALS at 250 K. 2D maps of the normalised TRPL data are shown in the left column, extracted spectra in the central column and extracted dynamics, normalised at 4 ns, in the right column. Initial exciton density varies from 10^{17}cm^{-3} (top row) through 10^{18}cm^{-3} (middle row) to 10^{19}cm^{-3} (bottom row).

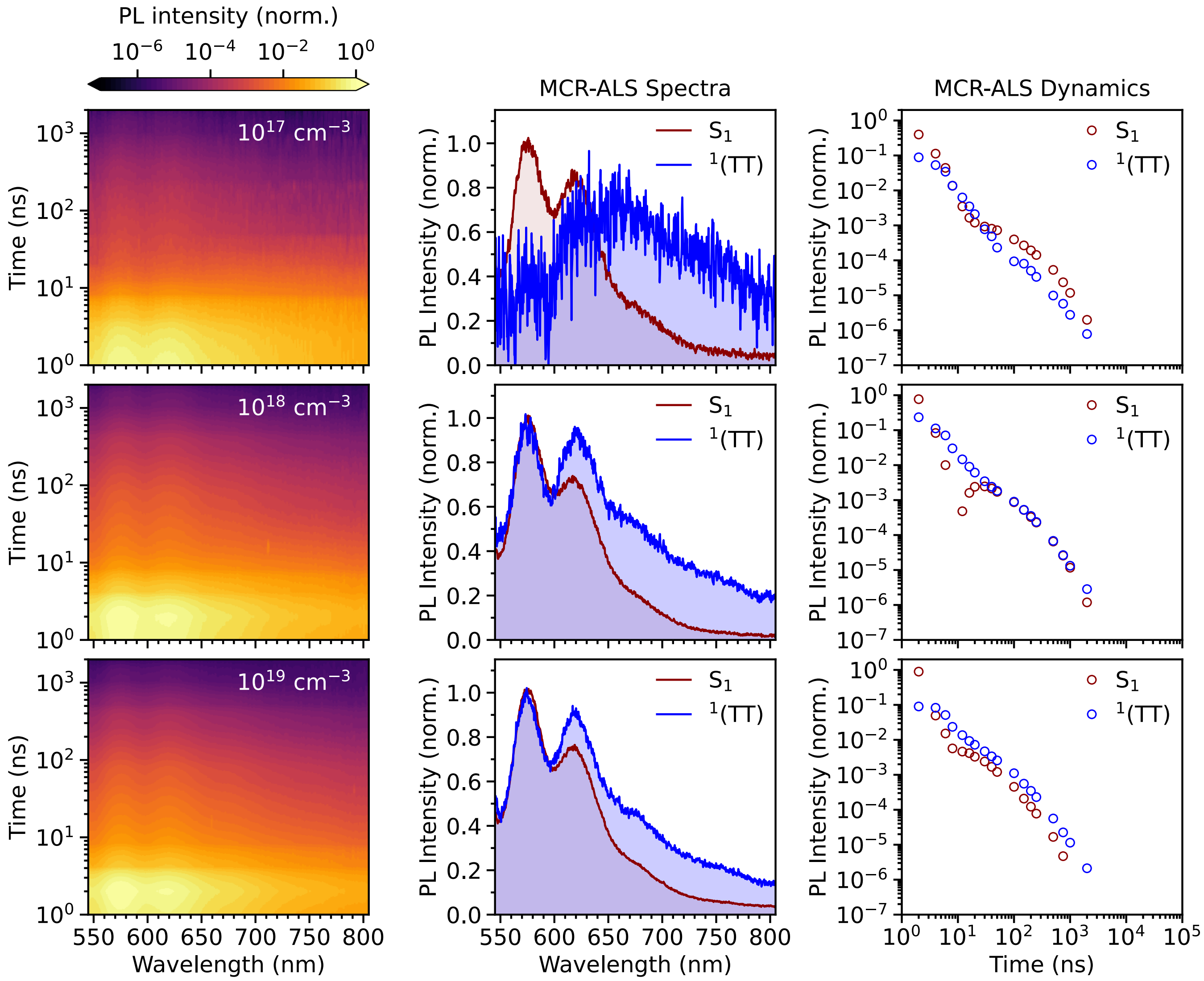

Figure 12 | Extraction of S_1 and ^{1}(TT) components by MCR-ALS at 291 K. 2D maps of the normalised TRPL data are shown in the left column, extracted spectra in the central column and extracted dynamics, normalised at 4 ns, in the right column. Initial exciton density varies from 10^{17}cm^{-3} (top row) through 10^{18}cm^{-3} (middle row) to 10^{19}cm^{-3} (bottom row).

5 Transient absorption of diftes

Figure 13a shows transient absorption (TA) spectra of a dilute solution of diftes (10^{-4}M in anhydrous toluene, sealed under nitrogen atmosphere inside a 1 mm path length quartz cuvette). All excited state absorption, ground state bleach and stimulated emission features decay mono-exponentially with a time constant of ∼12 ns (Figure 13b). They are therefore assigned to the singlet exciton.

Figure 13c shows TA spectra of a diftes thin film. The spectra are broadly similar to those found in dilute solution, yet now there are spectral changes with time, indicating that more than one species is present (for example, compare 430 nm with 495 nm at 1 ps and 1 ns). To begin with everything decays with a time constant of 100 ps (Figure 13d); this is attributed to singlet fission which rapidly depletes the singlet exciton population. We speculate that a longer lived species evident at 495 nm arises from triplet-pairs. Note that the oscillations in the TA spectra present in the NIR arise from optical interference effects related to the encapsulating glass coverslip.

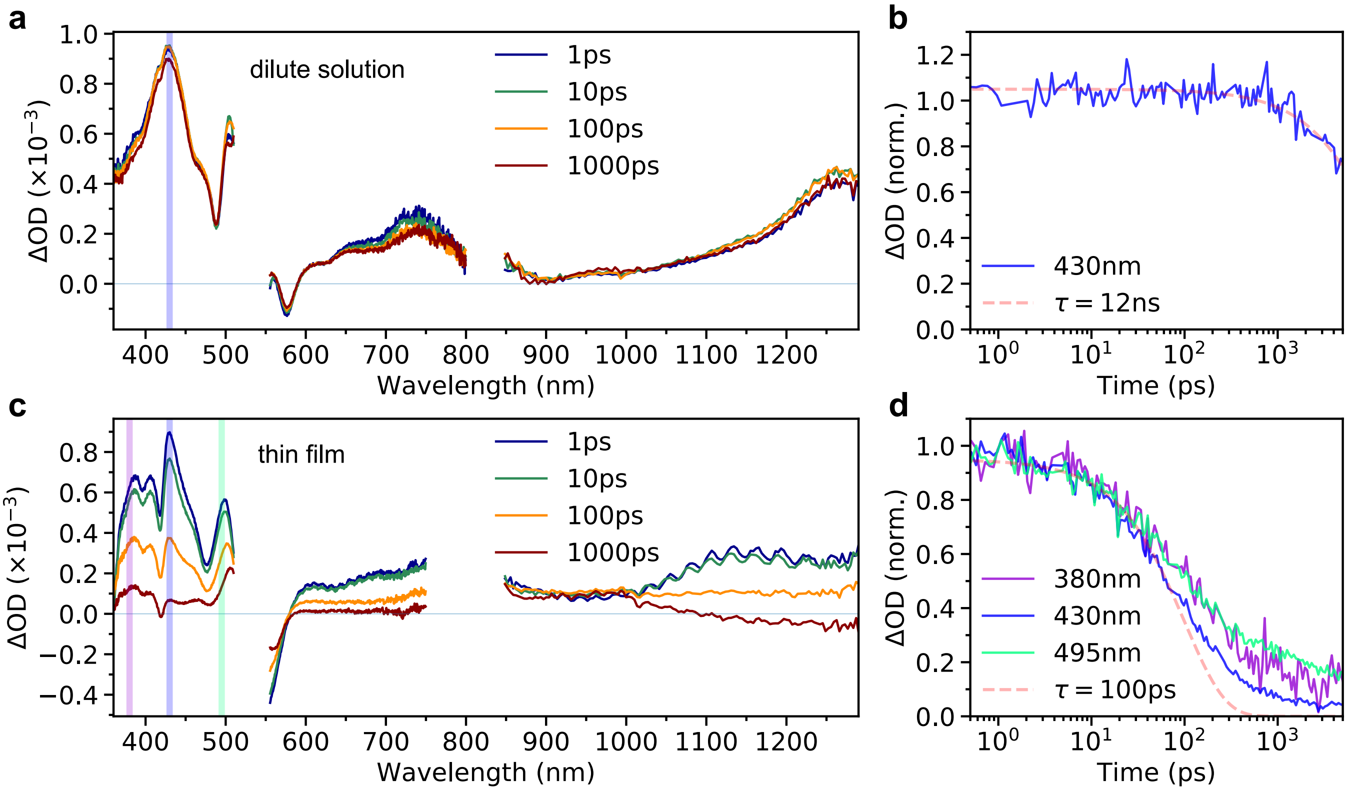

Figure 13 | Transient absorption of diftes. a, TA spectra of dilute solution. **b** Dynamics at 430 nm, corresponding to the singlet exciton. **c**, TA spectra of a diftes thin film. **d**, TA dynamics captured at various wavelengths (indicated by coloured bars in **c**), showing fast singlet fission (100 ps) followed by longer lived triplet-pairs (evident at 495 nm). Note that the spectral region around 532 nm has been removed due to pump scatter.

6 Kinetic modelling for diftes

Full details of the kinetic modelling procedures are provided in the Methods.

6.1 Merrifield's model

The most well known kinetic model of singlet fission was originally proposed by Johnson and Merrifield in 1970 in order to explain the changes in prompt and delayed luminescence with applied magnetic field in anthracene crystals[8]. We briefly summarise the key points of the model below. For a more detailed discussion, readers are directed to a summarising article by Bardeen and co-workers[9], although it should be noted that the correct construction of the spin Hamiltonian can be found in work by Tapping and Huang[10].

If we consider a pair of adjacent molecules, A and B, the total spin operator of the resulting 4-electron system can be diagonalized in the 4-electron product basis to yield 16 solutions of which 2 have a total spin of 0 (singlet states), 9 have a total spin of 1 (triplet states) and 5 have a total spin of 2 (quintet states). The first of the two singlets is simply the product of 2-electron singlet states. The second, however, can be written as a linear superposition of product pairs of 2-electron triplet states. For example:

$$|\mathrm{S}_2^{(4)}\rangle = \frac{1}{\sqrt{3}}\Big(|x\rangle_A\,|x\rangle_B + |y\rangle_A\,|y\rangle_B + |z\rangle_A\,|z\rangle_B\Big) \tag{1}$$

where $|x\rangle_A$, $|y\rangle_A$ and $|z\rangle_A$ correspond to triplet states situated on molecule A in the zero-field basis and similarly for molecule B.

This spin wavefunction is an excellent approximation to that of a triplet-pair state for which there is no electronic interaction (i.e. no orbital overlap) between the constituent triplets[11]. Thus pairs of separated triplets can be formed from photo-excited singlets without flipping any spins, giving rise to ultrafast singlet fission. The central assumption in Merrifield's construction is that triplet pairs, '(TT)', have no electronic interaction. The strongly exchanged-coupled ^{1}(TT) is not included in this model.

Next we construct the spin Hamiltonian for the 4-electron system and diagonalize it in the zero-field basis of product triplet-pair states ($|x\rangle_A\,|x\rangle_B$, $|x\rangle_A\,|y\rangle_B$ etc.). This results in 9 spin eigenstates $|\phi_l\rangle$ with $l = 1 - 9$. These 9 triplet-pair states, denoted $(\mathrm{TT})^l$, can be projected onto the singlet spin wavefunction, thereby giving their singlet character C_S^l:

$$C_S^l = \frac{1}{\sqrt{3}}\Big(\langle xx| + \langle yy| + \langle zz|\Big)\,|\phi_l\rangle \tag{2}$$

The rates of interconversion between the singlet and the 9 $(\mathrm{TT})^l$ are proportional to $|C_S^l|^2$, which allows us to construct the kinetic scheme of Merrifield's model as follows:

$$\frac{d[\mathrm{S}_1]}{dt} = -\left(k_{sf}\sum_{l=1}^{9}|C_S^l|^2 + k_{snr}\right)[\mathrm{S}_1] + k_{-sf}\sum_{l=1}^{9}|C_S^l|^2[(\mathrm{TT})^l] \tag{3}$$

$$\frac{d[(\mathrm{TT})^l]}{dt} = k_{sf}|C_S^l|^2[\mathrm{S}_1] - \Big(k_{-sf}|C_S^l|^2 + k_{hop} + k_{ttnr}\Big)[(\mathrm{TT})^l] + \frac{1}{9}k_{tta}[\mathrm{T}_1]^2 \tag{4}$$

$$\frac{d[\mathrm{T}_1]}{dt} = 2k_{hop}\sum_{l=1}^{9}[(\mathrm{TT})^l] - 2k_{tta}[\mathrm{T}_1]^2 - k_{tnr}[\mathrm{T}_1] \tag{5}$$

Triplet-pair states can dissociate through k_{hop} to form pairs of free triplets which can subsequently annihilate with rate k_{tta} to re-form the triplet-pairs. This is a bimolecular, non-geminate process. Note that this process will populate the 9 triplet pair states with equal probability. Finally, the model includes decay of the excited states to the ground state through k_{snr}, k_{ttnr} and k_{tnr}, which in practice are the sum of the radiative and non-radiative rates.

We again highlight that one of the key assumptions underlying this model is that there is no electronic interaction between the triplets comprising each of the $(\mathrm{TT})^l$ states. We cannot therefore directly apply this model to datasets in which we clearly measure PL from two distinct singlet states, S_1 and ^{1}(TT). To start, therefore, we take the same approach as for pentacene (see main text). We use simple 3-state models that explicitly include ^{1}(TT). Finding these to be inadequate, and since we also wish to simulate magnetic field effects, we subsequently make modifications to Merrifield's model and find that simply by explicitly including ^{1}(TT) as an intermediate between S_1 and $(T..T)^l$, where $(T..T)^l$ are identical to Merrifield's $(TT)^l$, we are able to obtain a quantitative description of our full temperature- and excitation density-dependent TRPL (Section 6.3, Figure 16), as well as the room-temperature magnetic field effect (Section 7).

6.2 Simple 3-state models are insufficient for diftes

Figure 14a shows a schematic diagram of a simple 3-state model similar to that used to describe the excited-state dynamics in pentacene single crystals (see main text). The rate equations are as follows:

$$\frac{d[\mathrm{S}_1]}{dt} = -(k_{sf} + k_{snr})[\mathrm{S}_1] + k_{-sf}[^1(\mathrm{TT})] \tag{6}$$

$$\frac{d[^1(\mathrm{TT})]}{dt} = k_{sf}[\mathrm{S}_1] - (k_{-sf} + k_{ttnr} + k_{hop})[^1(\mathrm{TT})] + k_{tta}[\mathrm{T}_1]^2 \tag{7}$$

$$\frac{d[\mathrm{T}_1]}{dt} = k_{hop}[^1(\mathrm{TT})] - 2k_{tta}[\mathrm{T}_1]^2 - k_{tnr}[\mathrm{T}_1] \tag{8}$$

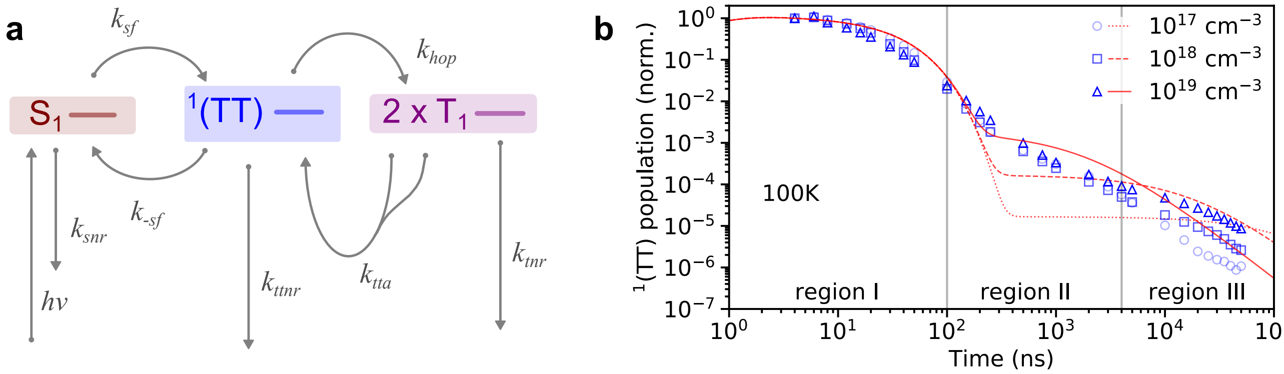

Figure 14 | The simplest possible 3-state model. **a**, Schematic diagram of the kinetic model. **b**, The simulated ^{1}(TT) population (red lines) fails to capture the 3 distinct regions of measured emission dynamics. The onset of excitation-dependence occurs immediately after the mono-exponential decay of region I, i.e. the model cannot simulate region II.

Figure 14b shows the result of attempting to fit this model to the measured decay of the ^{1}(TT) emission. Naturally, the initial portion of the data can be explained, however the model fails to capture the dynamics beyond 100 ns. Indeed, we find that it is only possible to generate regions I and III using this model, i.e. the initial exponential decay of the ^{1}(TT) population and the onset of an exciton density dependence arising from bimolecular TTA.

We suggest that the reason for the poor performance of the model is due to its inherent inability to consider geminate, monomolecular TTA as well as the non-geminate, bimolecular process. Put another way, with only a single 'triplet-pair' species explicitly included in the equations, there is no way to keep track of triplet-pairs that never fully separate. In this model, once ^{1}(TT) has separated to form two free triplets, any information regarding the origin of those two triplets is lost.

The simplest way to mimic the effect of geminate TTA might be to include a monomolecular pathway from free triplets to ^{1}(TT). Thus we add the process $T_1 + T_1 \rightarrow {}^1$(TT) to the kinetic scheme, but with a rate k_{-hop} that depends only linearly on the free triplet population (Figure 15a). The rate equations become:

$$\frac{d[\mathrm{S}_1]}{dt} = -(k_{sf} + k_{snr})[\mathrm{S}_1] + k_{-sf}[^1(\mathrm{TT})] \tag{9}$$

$$\frac{d[^1(\mathrm{TT})]}{dt} = k_{sf}[\mathrm{S}_1] - (k_{-sf} + k_{ttnr} + k_{hop})[^1(\mathrm{TT})] + k_{-hop}[\mathrm{T}_1] + k_{tta}[\mathrm{T}_1]^2 \tag{10}$$

$$\frac{d[\mathrm{T}_1]}{dt} = k_{hop}[^1(\mathrm{TT})] - 2k_{tta}[\mathrm{T}_1]^2 - (2k_{-hop} + k_{tnr})[\mathrm{T}_1] \tag{11}$$

Applying this scheme to our data, we find that, just as for the first model, it is unable to reproduce the dynamics beyond 100 ns (Figure 15b). It would seem that simply including a monomolecular pathway from free triplets to triplet-pairs is not a reasonable approximation to geminate recombination.

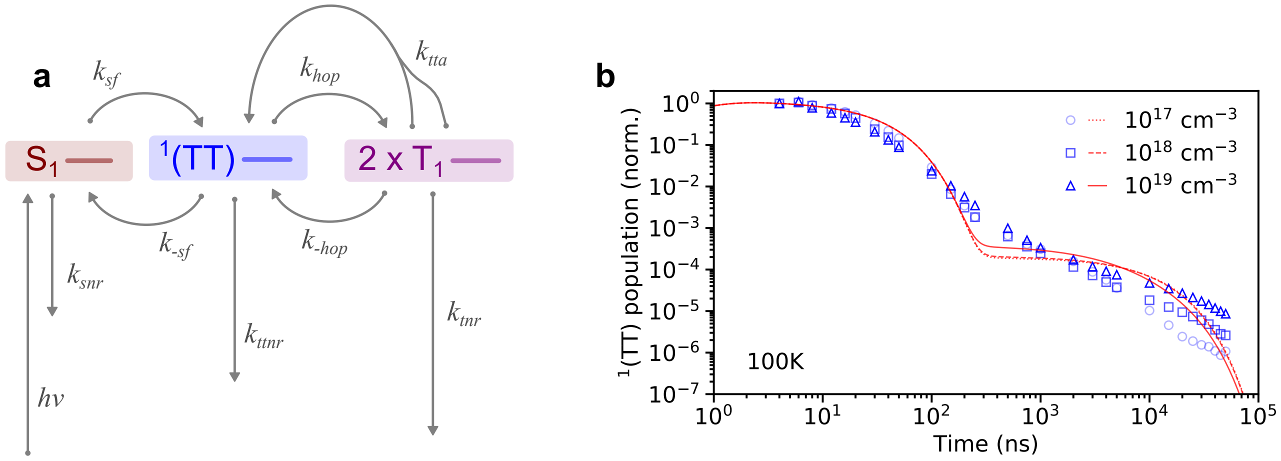

Figure 15 | Simple inclusion of geminate triplet recombination. **a**, Schematic diagram of the kinetic model: the same as above but including a monomolecular triplet recombination pathway. **b**, The simulated ^{1}(TT) population (red lines) still fails to capture the 3 distinct regions of measured emission dynamics. Together with Figure 14, this suggests that an additional excited state species is required in the kinetic scheme in order to successfully reproduce the excited state dynamics.

6.3 Explicit inclusion of ^{1}(TT)

Note that this is the model presented in the main text for diftes.

We noted above that the $(\mathrm{TT})^l$ states of Merrifield's model have no electronic interaction, the implication being that there is no orbital overlap between the constituent triplets. The strongly interacting ^{1}(TT) is not included. Therefore, by explicitly including a ^{1}(TT) population in Merrifield's kinetic model, the $(\mathrm{TT})^l$ states take on the role of the intermediate, non-interacting triplet-pairs ($(\mathrm{T..T})^l$). Following Bardeen[9], we allow for spin relaxation amongst the $(\mathrm{T..T})^l$ states, and include a rate k_{hop2} which represents the complete separation of triplet-pairs. Figure 16 shows a schematic diagram of this model, and the governing equations are presented below.

$$\frac{d[\mathrm{S}_1]}{dt} = -\left(k_{sf} + k_{snr}\right)[\mathrm{S}_1] + k_{-sf}[^1(\mathrm{TT})] \tag{12}$$

$$\frac{d[^1(\mathrm{TT})]}{dt} = k_{sf}[\mathrm{S}_1] - \left(k_{-sf} + k_{hop}\sum_{l=1}^{9}|C_S^l|^2 + k_{ttnr}\right)[^1(\mathrm{TT})] + k_{-hop}\sum_{l=1}^{9}|C_S^l|^2[(\mathrm{T..T})^l] \tag{13}$$

$$\begin{aligned}\frac{d[(\mathrm{T..T})^l]}{dt} &= k_{hop}|C_S^l|^2[^1(\mathrm{TT})] - \left(k_{-hop}|C_S^l|^2 + k_{hop2} + k_{tnr} + k_{relax}\right)[(\mathrm{T..T})^l] \\ &\quad + \frac{1}{8}k_{relax}\sum_{j\neq l}[(\mathrm{T..T})^j] + \frac{1}{9}k_{tta}[\mathrm{T}_1]^2\end{aligned} \tag{14}$$

$$\frac{d[\mathrm{T}_1]}{dt} = \left(k_{tnr} + 2k_{hop2}\right)\sum_{l=1}^{9}[(\mathrm{T..T})^l] - 2k_{tta}[\mathrm{T}_1]^2 - k_{tnr}[\mathrm{T}_1] \tag{15}$$

We find that this relatively simple modification of Merrifield's model is able to reproduce our experimentally determined exciton density-dependent ^{1}(TT) population dynamics with a high degree of accuracy, at all temperatures measured (Figure 16b-g). The Merrifield model is therefore almost sufficient to describe the singlet fission dynamics of diftes. Explicit inclusion of the ^{1}(TT) population is the significant modification required in order to successfully reproduce our kinetic dataset. In doing so, we separate the ultrafast electronic process $\mathrm{S}_1 \rightarrow {}^1(\mathrm{TT})$ from the slower loss of electronic interaction between triplet-pairs, which is governed by triplet hopping. Using this successful kinetic scheme, which also reproduces the measured effects of magnetic field on PL (see Section 7) we are able to learn more about triplet-pair dynamics by examining the temperature dependence of the various rate constants.

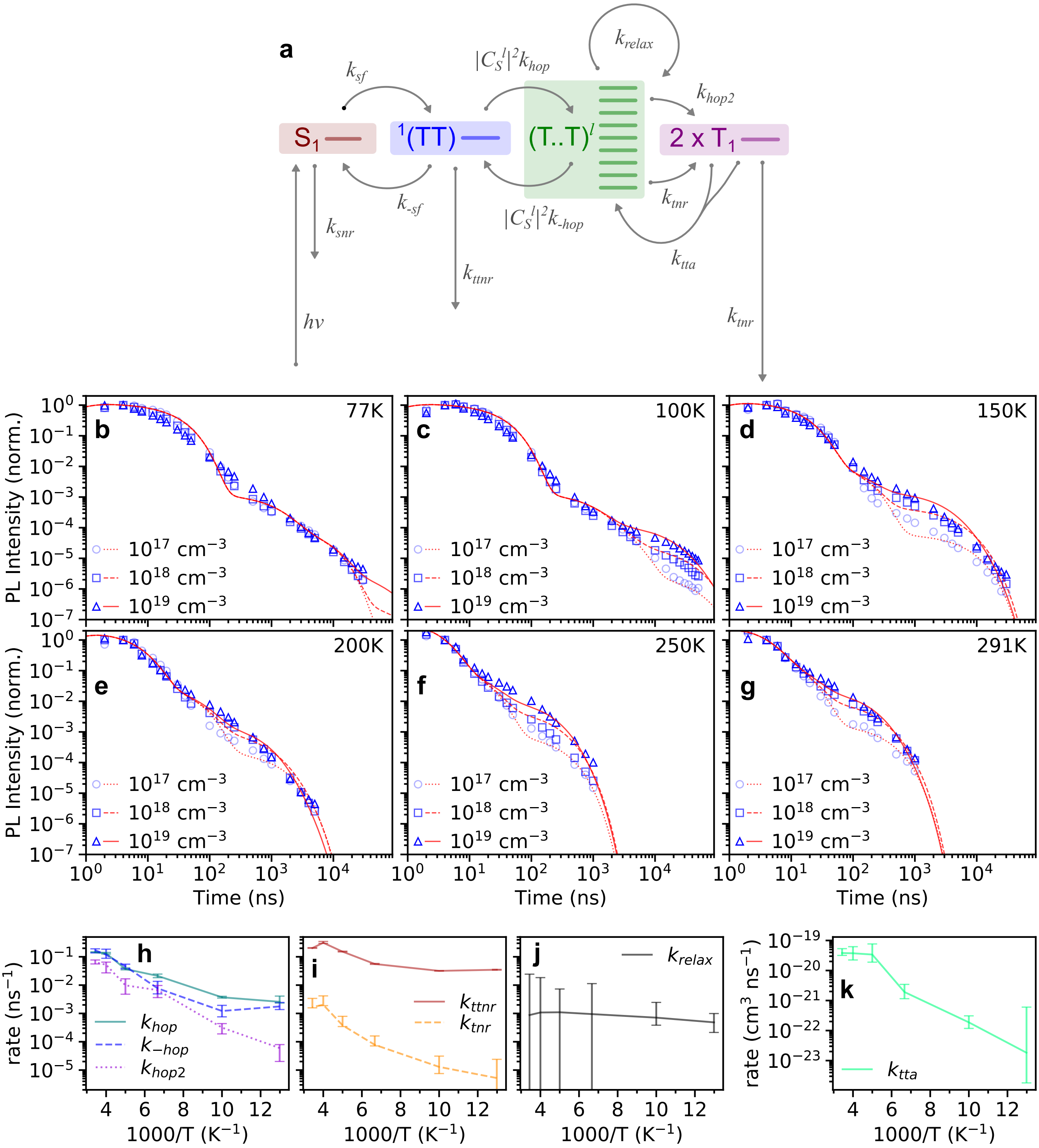

Figure 16 | **^{1}(TT) population dynamics in diftes.** **a**, Schematic diagram of the kinetic model. **b-g**, Measured ^{1}(TT) population dynamics as function of exciton density and temperature (blue symbols) together with the simulated population using the kinetic scheme illustrated above (red lines). The kinetic scheme accurately reproduces the excitation density-dependent dynamics across all six temperatures. **h-k**, rate constants extracted from the kinetic modelling as a function of temperature. **h**, Triplet hopping rates, **i**, Non-radiative rates, **j**, Spin-lattice relaxation rate (same vertical scale) and **k**, Triplet-triplet annihilation rate constant. All the rate constants display plausible temperature dependencies. Uncertainty in the rate constants, reflected here by the error bars, is discussed in Section 6.5.

6.3.1 diftes films may offer a unique insight into triplet-pair dynamics

Many of the time-resolved photoluminescence measurements that have been performed on SF materials and combined with kinetic or density matrix modelling have tracked the population of the singlet exciton S_1[8,12–16]. ^{1}(TT) population dynamics are typically extracted from transient absorption data through global or target analysis[6,17,18] but it becomes difficult when, for example, ^{1}(TT), $(T..T)^l$ and T_1 all have very similar excited-state absorption spectra[19]. Furthermore, signal-to-noise limitations of transient absorption mean that, at best, only the first 3 orders of magnitude of population decay can be measured. While this may be sufficient to capture the dominant 'forward' dynamics, the finer details of the interactions and equilibrium between triplet-pair species are obscured.

We have demonstrated that, at low temperature, diftes thin films exhibit remarkably bright photoluminescence from the ^{1}(TT) state which can be tracked over many orders of magnitude using highly sensitive time-resolved photoluminescence techniques. As a simple example of the potential that diftes has as a model system for investigations of triplet-pair states, we can examine the behaviour of various rate constants as a function of temperature (Figure 16h-k). Firstly, we note that the large error bars for k_{hop2} and k_{tta} at 77 K reflect the fact that complete triplet-pair dissociation is largely suppressed at this temperature. Strikingly, we find that the forwards and backwards rates for triplet-pair separation, k_{hop} and k_{-hop}, are nearly equal at every temperature (Figure 16h). According to the principle of detailed balance, this implies a near-zero difference in free energy between ^{1}(TT) and $(T..T)^l$. If, as widely claimed[20], there is an entropic gain for free triplet formation, then the electronic energy of the ^{1}(TT) state must be lower than $2 \times E_{T_1}$.

As shown in Figures 16h and 16k, the hopping rates follow a qualitatively similar temperature dependence to the TTA rate constant k_{tta}, which suggests that all of these processes are governed by triplet hopping.

We suggest that diftes, measured at low temperature, is an ideal system in which to study the fundamentals of triplet-pair states. At 100 K we observe clearly separated regimes in which strongly-coupled triplet-pairs, weakly-coupled triplet-pairs and finally free triplets dominate the population dynamics, meaning that investigations into triplet-pair separation mechanisms and spin coherences could be particularly illuminating, especially given the recent excitement surrounding the entangled nature of triplets produced through SF[21].

6.4 Spin-lattice relaxation has little effect

Finally, we remove the process of spin-lattice relaxation in order to see how much of an effect this has on the model's ability to reproduce the experimental data. A schematic of the resulting kinetic scheme is shown in Figure 17a and the fitted results are shown in Figure 17b-g. The quality of the fit is almost unchanged, despite having one less parameter to vary.

The temperature dependencies of the rate constants (Figure 17h-j), are also very similar. The principal difference is the value of k_{tta} at 77 K. Since complete separation of triplet-pairs is largely suppressed at this temperature (lack of exciton density dependence in the dynamics) the rate of free triplet annihilation is in any case not well defined.

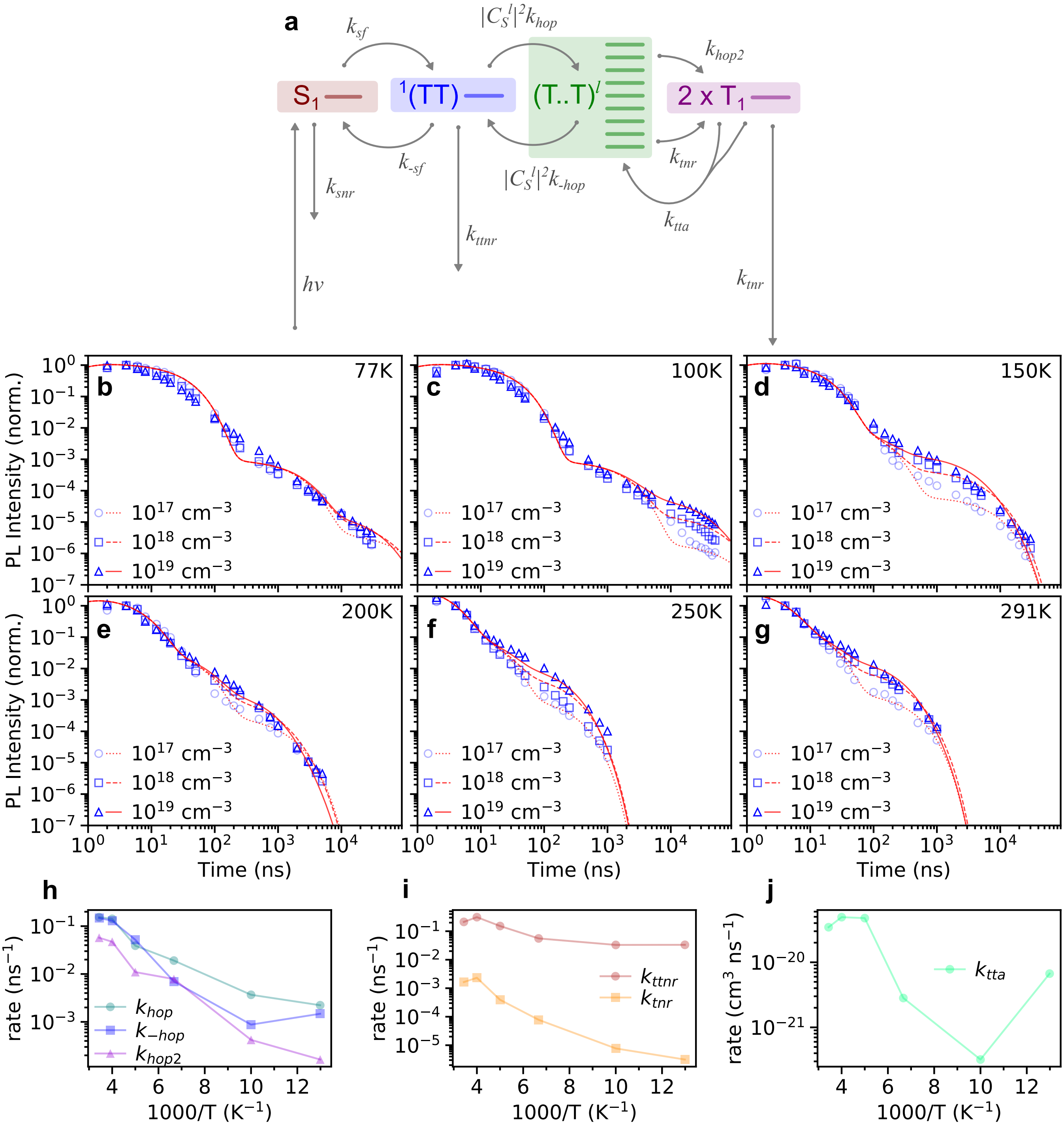

Figure 17 | Spin-lattice relaxation has only a small effect on the kinetic model outlined in the main text. a, Schematic of the kinetic model. It is identical to the previous figure, except that spin-lattice relaxation is not included. **b-g**, Application of the model (red lines) to the TRPL data (blue markers). The model is able to adequately describe the data even with one fewer free parameters. **h-k**, Extracted rate constants as a function of temperature.

6.5 Uncertainty estimation for rate constants

Uncertainty in each rate constant (for the kinetic model presented in the main text and Section 6.3) was estimated by individually varying each one about its optimised (or fixed) value, whilst keeping all others constant and monitoring the effect on a cost function. The cost function, χ, was the same as was minimised during the rate constant optimisation process and was defined as:

$$\chi = \frac{1}{2N} \sum_{i=1}^{N} (\log_{10} y_i - \log_{10} f_i)^2 \tag{16}$$

where $i = 1, 2, ..., N$ runs over every time point at all three exciton densities measured and y_i and f_i are the measured and simulated ^{1}(TT) populations respectively. The normalisation by N is included to allow comparison between cost functions at different temperatures, for which different numbers of time points were measured. The logarithms were taken in order to give equal weight across all timescales measured.

The uncertainty in each rate constant was calculated as the lower and upper values which caused an increase of 20% in the cost function. The choice of 20% as a threshold is of course arbitrary, but it allows for a comparison of the uncertainties between rate constants.

Figures 18-23 on the following two pages illustrate the process for calculating the uncertainty in each rate constant for temperatures of 77 K to 291 K. Black lines show the variation of χ with each rate constant. The dashed horizontal grey line shows the value of the optimized cost function, the solid one shows the 20% threshold. Vertical grey lines indicate the optimised value for each rate constant. Red circles indicate the lower and upper bounds. Note that though shown, k_{sf}, k_{-sf} and k_{snr} were not varied during the optimisation.

Unsurprisingly, given that singlet fission is much faster than our instrument response, we find that the values of k_{sf}, k_{-sf} and k_{snr} have negligible effect on the model output. We further find that k_{relax} has no lower bound for temperatures above 100 K, which is to say that it only has a significant role at low temperature. In contrast, k_{hop}, k_{-hop}, k_{hop2}, k_{tta}, k_{ttnr} and k_{tnr} are generally very tightly constrained. Note that at 77 K there is very little dependence of the ^{1}(TT) decay with excitation density, indicating that complete triplet separation is largely suppressed at this temperature. As a result, k_{hop2} and k_{tta} are relatively poorly constrained at 77 K.

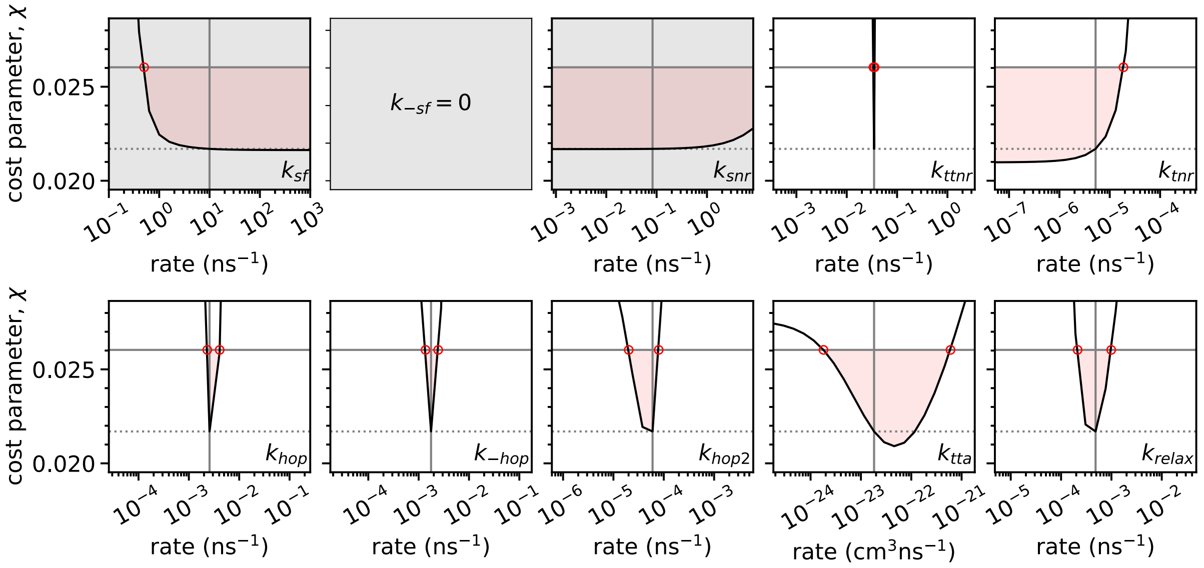

Figure 18 | Uncertainty estimation for the rate constants in the kinetic model presented in the main text at 77 K. Note that k_{-sf} is not included in the analysis since it was set to zero. Grey shading indicates rate constants that were not varied. Each rate constant was individually varied about its optimised value; uncertainty was estimated as the lower and upper values that caused a 20% increase in the cost parameter.

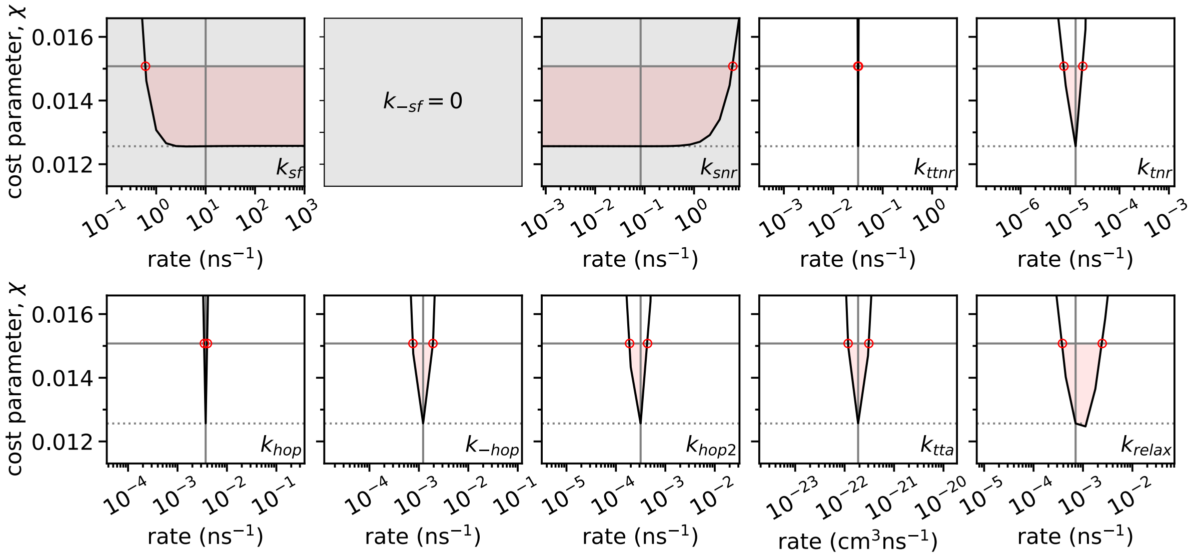

Figure 19 | Uncertainty estimation for the rate constants in the kinetic model presented in the main text at 100 K. Note that k_{-sf} is not included in the analysis since it was set to zero. Grey shading indicates rate constants that were not varied. Each rate constant was individually varied about its optimised value; uncertainty was estimated as the lower and upper values that caused a 20% increase in the cost parameter.

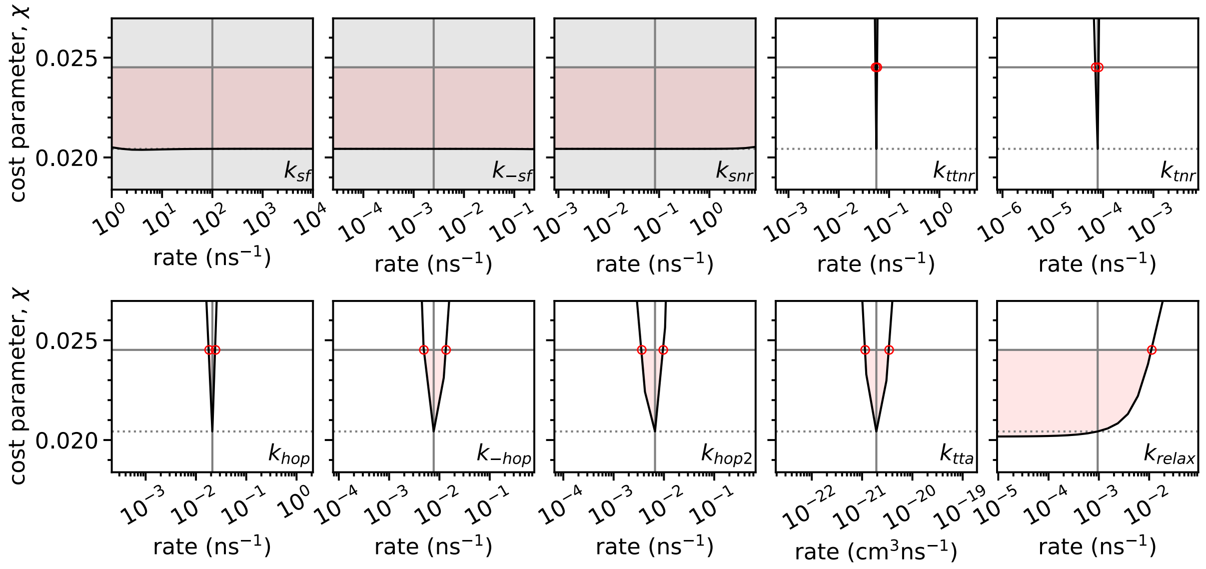

Figure 20 | Uncertainty estimation for the rate constants in the kinetic model presented in the main text at 150 K. Grey shading indicates rate constants that were not varied. Each rate constant was individually varied about its optimised value; uncertainty was estimated as the lower and upper values that caused a 20% increase in the cost parameter.

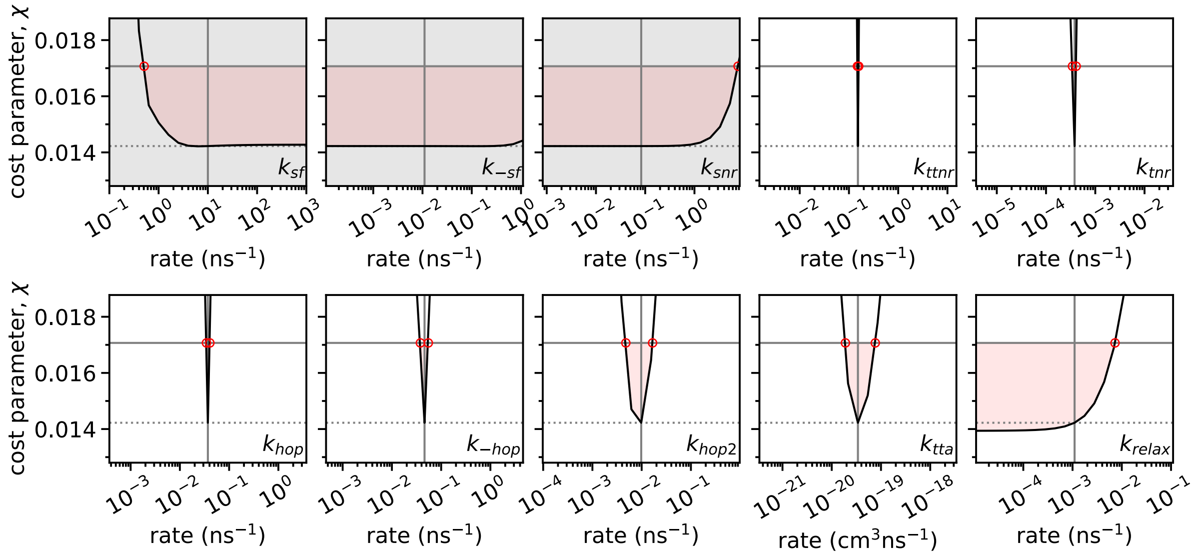

Figure 21 | Uncertainty estimation for the rate constants in the kinetic model presented in the main text at 200 K. Grey shading indicates rate constants that were not varied. Each rate constant was individually varied about its optimised value; uncertainty was estimated as the lower and upper values that caused a 20% increase in the cost parameter.

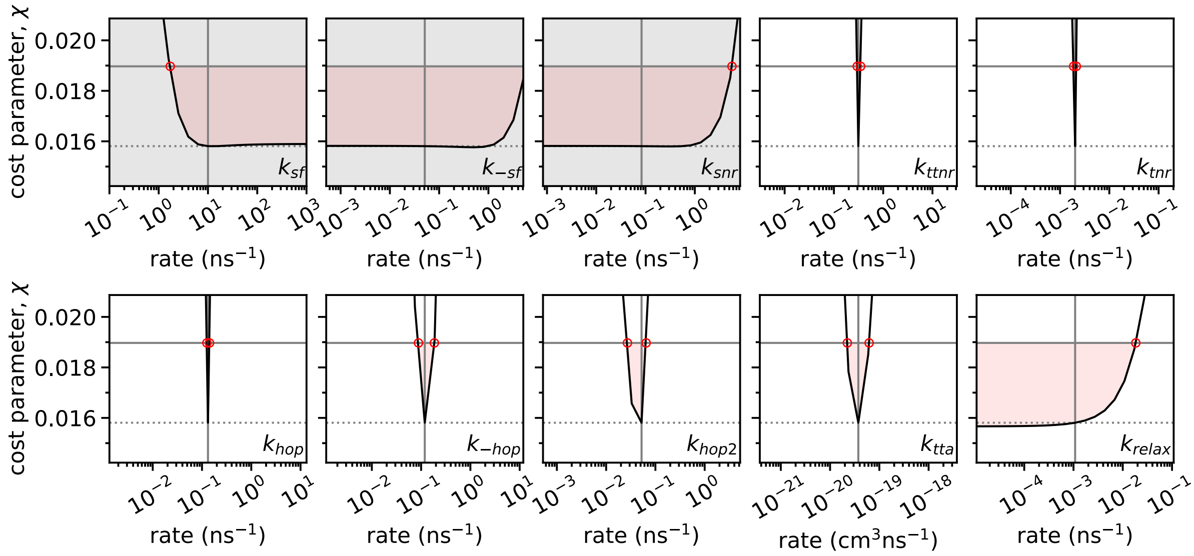

Figure 22 | Uncertainty estimation for the rate constants in the kinetic model presented in the main text at 250 K. Grey shading indicates rate constants that were not varied. Each rate constant was individually varied about its optimised value; uncertainty was estimated as the lower and upper values that caused a 20% increase in the cost parameter.

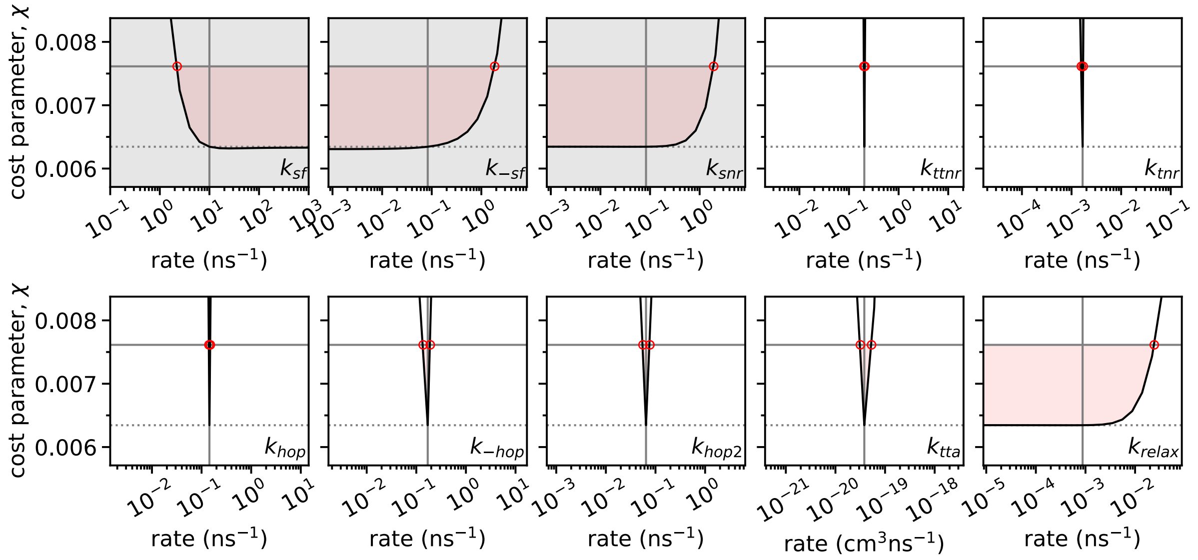

Figure 23 | Uncertainty estimation for the rate constants in the kinetic model presented in the main text at 291 K. Grey shading indicates rate constants that were not varied. Each rate constant was individually varied about its optimised value; uncertainty was estimated as the lower and upper values that caused a 20% increase in the cost parameter.

6.6 TTA does not populate ^{1}(TT) via S_1

In the case of pentacene, it is energetically impossible for two triplets to annihilate and form S_1. Indeed, this was the principal reason for which we measured ^{1}(TT) dynamics in pentacene. However, in the case of diftes there is no such energetic restriction. How, then, can we be sure that TTA in diftes does not populate S_1 which then undergoes fission to form ^{1}(TT)? This was the mechanism proposed for delayed excimer emission in concentrated TIPS-tetracene[22].

If we modify our favoured kinetic model (described in detail in the main text and Section 6.3) such that TTA populates S_1 rather than $(T..T)^l$, we find that we can still obtain a good fit to the experimentally measured ^{1}(TT) dynamics (Figure 24a). However, we would expect from the balance of rates that a small fraction ($< 1/120$) of S_1 excitons formed from TTA should decay radiatively, rather than undergoing fission. Yet since the radiative rate of S_1 is approximately 40 times greater than that of ^{1}(TT) in diftes[6], this would still lead to an appreciable S_1 contribution to the total PL of around 14% (Figure 24a, black lines) on timescales of tens of microseconds, which we do not observe (Figure 24b). We therefore conclude that, as is the case for pentacene, TTA populates the triplet-pair states directly and not via S_1.

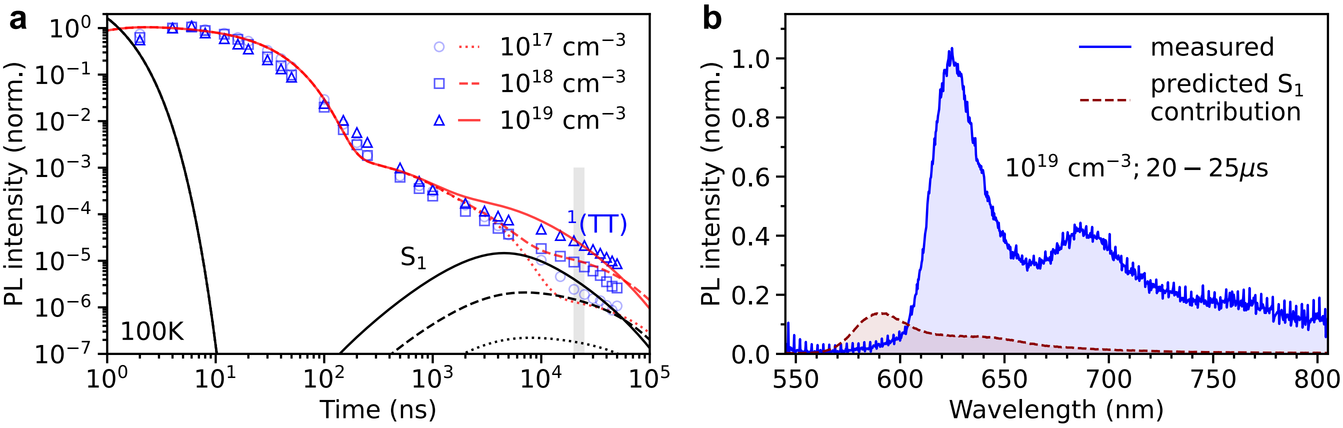

Figure 24 | TTA does not populate ^{1}(TT) via S_1. a, ^{1}(TT) dynamics can be reproduced using a kinetic model in which TTA populates S_1 directly rather than triplet-pairs. However, this would lead to an appreciable contribution to the total PL from S_1 (black lines) on long timescales which we do not observe. **b** shows the measured PL spectrum on a timescale of tens of microseconds. The PL arises entirely from ^{1}(TT); the predicted contribution from S_1 (red dashed line) is not observed.

6.6.1 Triplet sensitisation of diftes

We attempted to gain further confirmation that ^{1}(TT) is formed through bimolecular TTA by conducting triplet sensitisation experiments. The aim of these experiments was to add weight to the conclusion that bimolecular TTA does not proceed via S_1. Due to a variety of difficulties, outlined below, the experiments were not nearly as conclusive as we had hoped.

Methods

We added a small mole fraction ($\sim 1/250$) of the triplet sensitizer palladium (II) octabutoxyphthalocyanine ($PdPc(OBu)_8$)[23] to our $15\,\mathrm{mg\,ml^{-1}}$ diftes solution in toluene and spin-coated films using exactly the same method as for pure diftes films (see Methods). $PdPc(OBu)_8$ ($E_{T_1} = 1.24\,\mathrm{eV}$) has been shown to effectively sensitise triplets in rubrene ($E_{T_1} = 1.14\,\mathrm{eV}$)[23]. For the case of diftes ($E_{T_1} = 1.08\,\mathrm{eV}$[6]), triplet energy transfer is expected to be exothermic by approximately 160 meV.

Narrowband pump pulses at 725 nm were generated by frequency doubling the 1450 nm output of an optical parameteric amplifier (TOPAS Prime, Light Conversion) seeded with 800 nm pulses from a Ti:Sapphire regenerative amplifier (Solstice, Spectra Physics) in a BBO crystal. These pulses were then passed through:

- A KG3 filter, to remove residual IR
- An off-axis 750 nm bandpass filter, to spectrally clean the pulses
- A 695 nm longpass filter, to ensure that no wavelengths that could directly excite diftes were present in the pulse

Time-gated PL spectra were again measured using our iCCD detector (see Methods). A 700 nm shortpass filter (FES700, Thorlabs) was used to reduce scattered pump light.

Control for 2-photon absorption

725 nm light is well below the optical gap of diftes, but sufficient to excite the $S_0 \rightarrow S_1$ transition of PdPc(OBu)$_8$. We controlled for 2-photon absorption by repeating our measurements on a pure diftes film. This turned out to be important: using femtosecond pulses resulted in significant upconverted emission arising from 2-photon absorption even in the pure diftes film. We highlight that upconversion emission from 2-photon absorption can carry the same quadratic intensity dependence as that expected from bimolecular TTA. We therefore passed the 725 nm pump light through a 10 cm quartz rod and 2 m optical fibre to temporally stretch the pulses. As a result of this modification, we were able to measure upconverted emission only in the diftes film doped with PdPc(OBu)$_8$ and not in the pure film (Figure 25b).

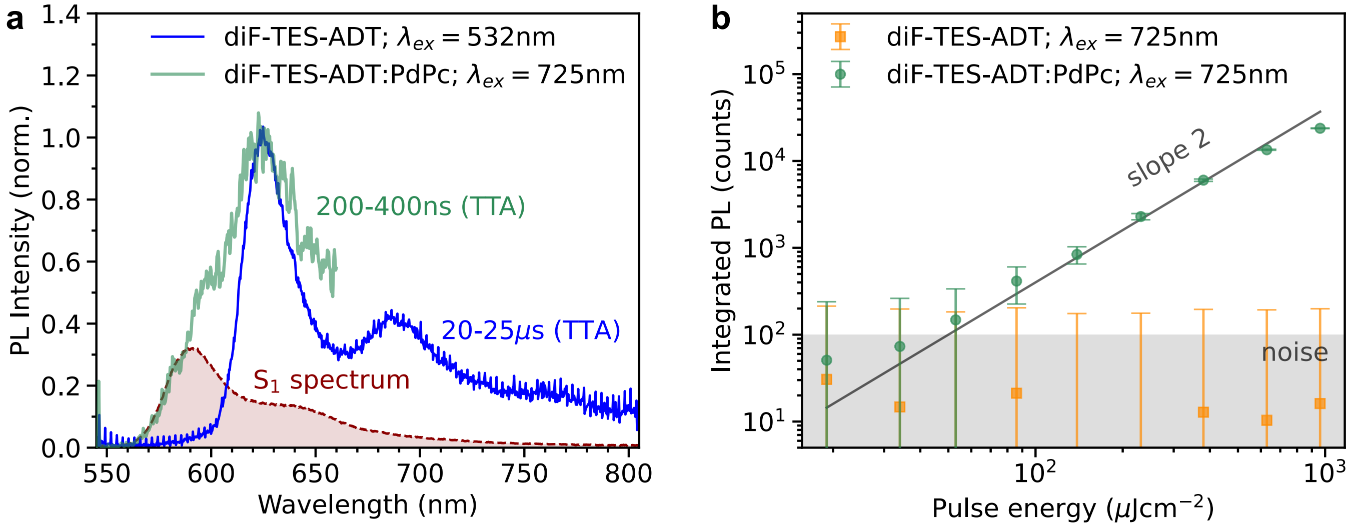

Figure 25 | Sensitised TTA in diftes thin films. **a**, Spectrum of upconverted emission (green line) compared to prompt (red dashed line) and delayed (blue line) PL in diftes at 100 K. The upconverted PL contains contributions from both S$_1$ and ^{1}(TT). The S$_1$ contribution is likely to arise from exothermic triplet transfer from a sensitiser aggregate onto a neighbouring diftes molecule that has already received a triplet. The excess energy then allows S$_1$ to be accessed. **b**, The dependence of the upconverted PL on pulse energy shows the expected quadratic relationship. No upconverted PL was observed in pure diftes films allowing us to rule out 2-photon absorption effects.

Results

Figure 25a shows spectra from pure diftes pumped at 532 nm. The prompt emission (red) arises predominantly from S$_1$, whilst that at 20 µs is from ^{1}(TT) at a time delay where bimolecular TTA dominates (blue). The upconverted emission, gated from 200–400 ns, arising from sensitised TTA (green) contains contributions from both S$_1$ and ^{1}(TT). Figure 25b shows the dependence of upconverted emission on laser power. The slope is 2, but no emission was observed for the pure film, confirming that TTA upconversion is the mechanism at play.

Discussion

The two spectra that arise from TTA are different: in the sensitisation experiment, a small amount of emission from S$_1$ is present, in addition to the expected ^{1}(TT) emission. This is consistent with the scenario presented in the preceeding section, whereby the annihilation of two triplets forms an S$_1$ state that subsequently undergoes exciton fission to produce ^{1}(TT). Indeed, running the same model shown in Figure 24a, yet starting with an initial population of triplets rather than singlets to mimic the sensitisation, yields an expected 14% contribution of S$_1$ to the total PL on a timescale of 200–400 ns, similar to the contribution shown in Figure 24a. This is similar to what we observe in Figure 25a.

How, then, does the discrepancy arise between the two 'TTA' spectra (blue and green lines in Figure 25a)? We propose that different, non-bimolecular TTA events dominate the recombination in the sensitised film. It is well known that porphyrin or phthalocyanine based triplet sensitisers aggregate and undergo phase separation when blended into crystalline films[24–26] and that this can be a major problem in solid-state upconversion systems leading to, for example, sensitiser-sensitiser annihilation and triplet quenching[25,26].

It is therefore quite likely that in our film, TTA occurs predominantly at these aggregates and may include contributions from sensitiser-sensitiser and sensitiser-acceptor TTA. In both of these cases, since triplet transfer from $\mathrm{PdPc(OBu)_8}$ to diftes is exothermic by approximately 160 meV, annihilation events carry more than enough excess energy to enable the $^1(\mathrm{TT}) \rightarrow \mathrm{S}_1$ transition, which is thermally activated in diftes, as demonstrated here and in previous work[6].

In an attempt to alleviate this problem of 'hot' TTA, we turned to a different type of triplet sensitiser: inorganic quantum dots (QDs) (sometimes called colloidal semiconductor nanocrystals)[27,28]. Colloidal PbS QDs possessing exceptionally narrow linewidths and with their triplet energies tuned to be equal to or very slightly above that of diftes were synthesised by Philippe Green in the group of Professor Mark Wilson at the University of Toronto, following the methods in their recent publication[29]. We fabricated two types of samples by either (1) blending a small molar fraction of the QDs in solution with diftes before spin coating or (2) spin-coating a thin layer ($\sim$ 5 dots) of QDs onto the substrate and thermally evaporating the same thickness $\sim$ 60 nm of diftes on top, forming a bilayer.

The QD-diftes samples were excited using the 1064 nm fundamental of our sub-ns Q-switched Nd:YVO4 laser (Picolo-AOT, Innolas). The films were maintained at 100 K in the same cryostat-PL setup described in the Methods. However, we were unable to measure any upconverted emission from any of the samples. We suspect that this may be due to very poor triplet transfer from the QD to the diftes, which is well known to be hindered by the oleic acid ligands that are attached to the surface of the QDs[30]. Further experiments using the QDs are ongoing.

7 Magnetic field effect in a diftes crystal

7.1 Methods

Full details of the sample preparation and magnetic-field dependent PL measurement are given in the Methods.

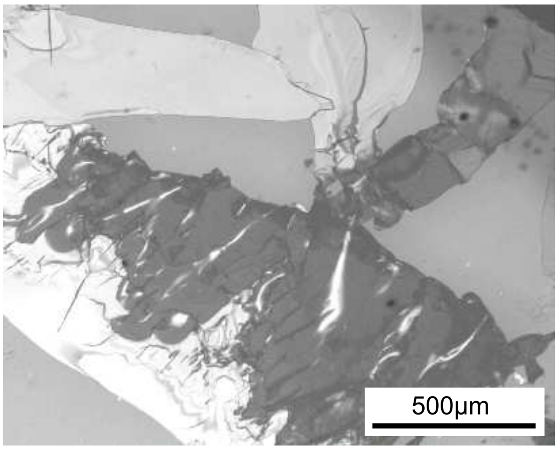

Figure 26 | Polarised micrograph of drop-cast diftes. Rather than forming a thin film, diftes crystallised into large domains scattered over the substrate. Viewed through crossed polarisers, we see that these crystalline domains are single-orientation and many hundreds of micrometers in size. Thus we conclude that our laser spot (50 µm diameter) sampled a single crystalline domain during the measurement. Note that medium grey areas (such as the bottom left corner) are bare substrate.

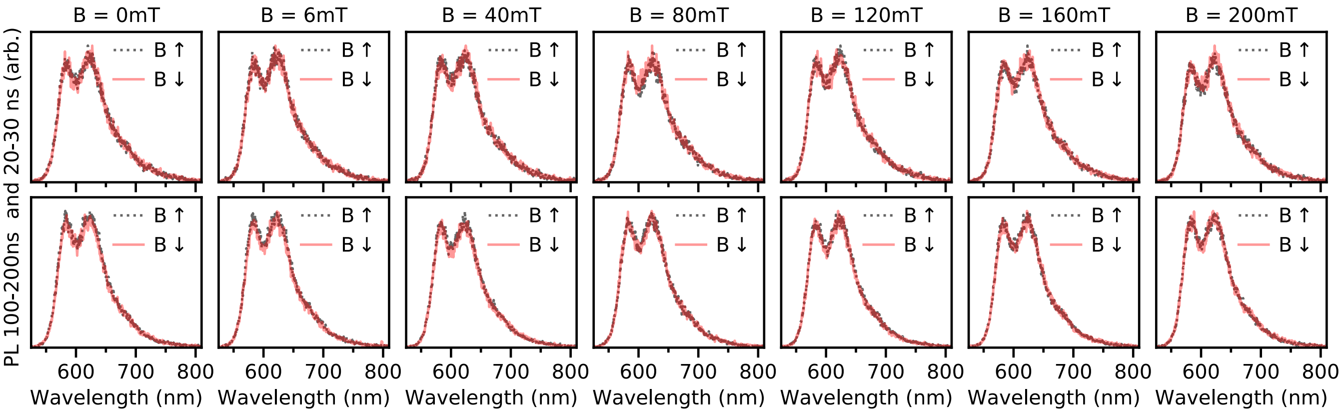

Figure 27 | Reproducability of the magnetic field effect. Spectra obtained while sweeping upwards in magnetic field (grey dots) exactly match in shape and magnitude those obtained as the magnetic field was reduced back down to zero (pink lines). Thus we are able to rule out photo-degradation and laser power fluctuation effects. The differences between measured PL counts upon sweeping up and down in magnetic field were used to calculate the error bars displayed in Figure 4c of the main text.

7.1.1 Simulation

The calculation of $|C_S^l|^2$ values outlined in Section 6.1 carries a magnetic field dependence. Thus the rate model can simulate the emission dynamics as a function of magnetic field. Since both S_1 and ^{1}(TT) contribute to the total PL signal at room temperature, we calculate the total emission dynamics from the sum of these two populations, weighted by their respective radiative rates, though since they are an equilibrium this has no effect on the normalised simulation output. Rate constants were initially taken from the room temperature kinetic models of the film emission dynamics. We found that the crystal emission dynamics were very similar, except for being longer-lived on long timescales, which we could reproduce simply by setting the free triplet decay rate to zero (panel a in the figures below). A longer triplet lifetime is expected for a highly crystalline sample. We then optimised the rate constants to obtain the best possible fit to the crystal kinetics (panel b in the figures below shows the percentage change in each rate constant). The simulated B-field-dependent emission dynamics were integrated over the windows of 20–30 ns and 100–200 ns to mimic the gating of our camera.

In the case of the diftes crystal domain for which the magnetic field effect was measured, we could not determine the orientation of the magnetic field with respect to the molecular axes. Instead, we assumed (001) packing, as suggested by the GIWAXS measurements described in Section 1.1. From the crystal structure[3], we then found the set of (θ, ϕ) values relating the B-field vector to the molecular axes that satisfied the constraint that the B-field vector should lie in the (001) plane. We sampled 21 sets of such values, and found a value ($\phi = 144°$) that best reproduced the measured magnetic field effect (panel c in the figures below). The variation with B-field vector orientation is shown in panel d of the figures below.

As described below, this procedure yielded an excellent fit to the kinetic data and also reproduced the shape of the MFE very well. However, the magnitude of the effect was overestimated by a factor of around 2. We therefore varied the parameters a little further, resulting in a slightly worse fit to the kinetic data but a near-perfect reproduction of the MFE (Figure 4c, main text). This procedure is described in Section 7.2.2 below.

7.2 Results

The results of the above procedure, using 2 different kinetic models, are shown in the following 2 figures. Figure 28 shows the results using the model described in the main text and Section 6.3 which is Merrifield's model, but explicitly including ^{1}(TT). In this case, excepting the magnitude, the magnetic field effect is well described by the model. Figure 29 shows the results using the model described in Section 6.6. This model is identical to that described in the main text and Section 6.3, except that annihilating triplets directly form S_1 rather than (T..T). In this case, again excepting the magnitude, the magnetic field effect is well described. We address the overestimation of magnitude below.

The rate model predicts almost the same ^{1}(TT) emission dynamics and room temperature magnetic field effect regardless of whether TTA is mediated by (T..T) or goes directly to S_1. On the timescales of our measurement, we are principally sensitive to the slower 'triplet' dynamics (the behaviour of ^{1}(TT), (T..T) and T_1). The magnetic field effect in particular probes the ^{1}(TT) $\leftrightarrow$ (T..T) interactions and is relatively insensitive to how ^{1}(TT) is formed in the first place. Instead, as described in Section 6.6, it is the lack of any S_1 emission in the delayed emission spectrum at 100 K that shows that TTA does not proceed directly via S_1. In addition, as explained in the main text, the delayed ^{1}(TT) emission arising from TTA in pentacene single crystals (for which S_1 is energetically inaccessible) shows that ^{1}(TT), not S_1, is a direct product of TTA.

The subsequent section illustrates the importance of considering separate S_1 and ^{1}(TT) states in the kinetic modelling of diftes. We apply Merrifield's model (Section 6.1) and show that whilst a good description of the 'singlet' emission dynamics at zero field is obtained, the model cannot reproduce the magnetic field effect on longer timescales.

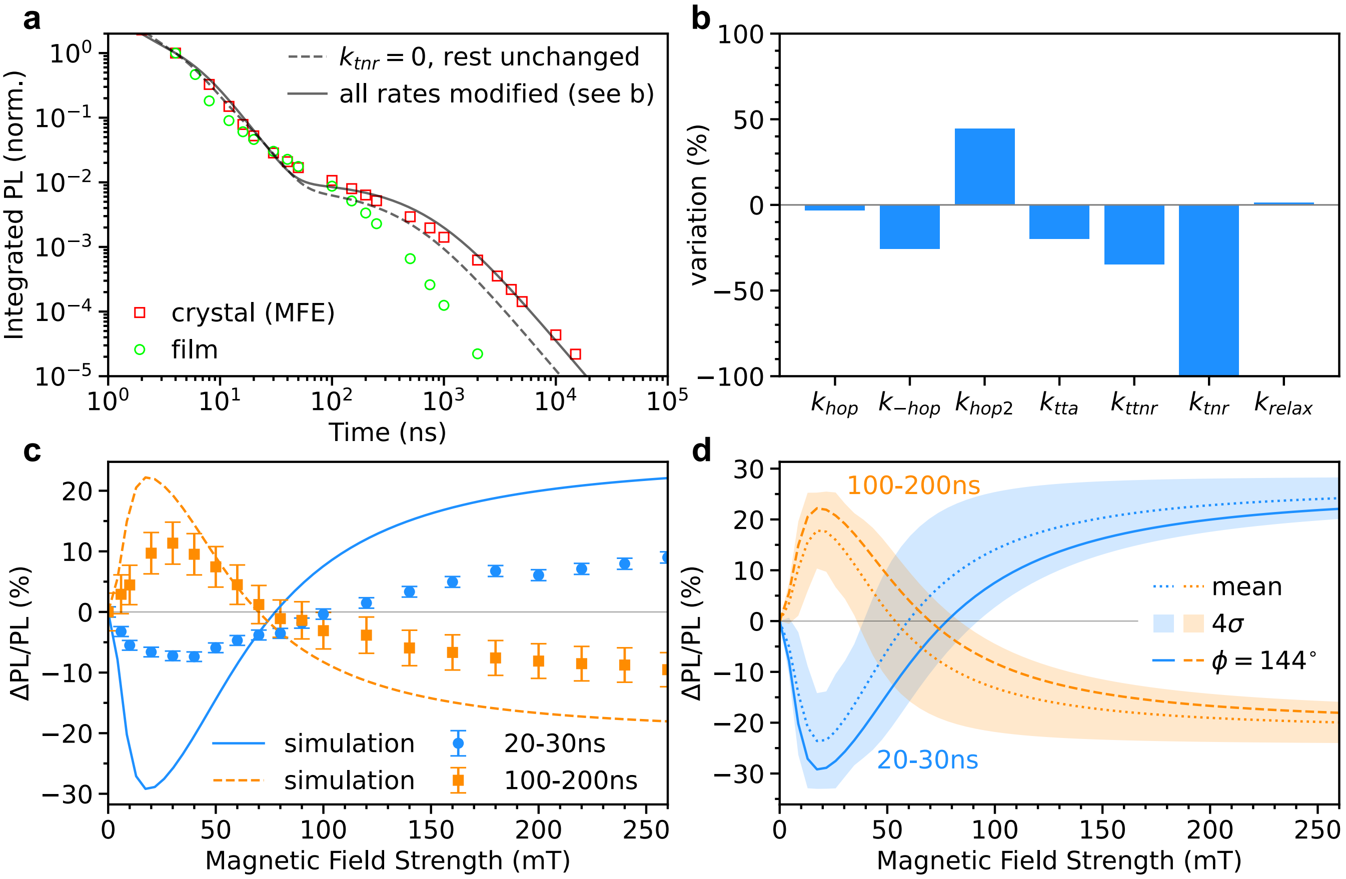

Figure 28 | Magnetic field effect on diftes single-crystal PL using the model presented in the main text. a, Kinetics of the crystal (red) are longer lived than the film (green) beyond 100 ns. This is explained by an enhanced triplet lifetime (much smaller k_{tnr}) in the crystal. Using the same rate constants as for the film, but setting $k_{tnr} = 0$ (dashed line), we reproduce the crystal emission dynamics. For calculation of the magnetic field effect, rate constants were slightly optimised, yielding a better fit to the emission dynamics (solid line). **b**, Change in optimised rate constants compared to their initial (film) values. **c**, Measured (markers) and simulated (lines) magnetic field effect, using the model described in Section 6.3 and the main text. Excepting the overall magnitude, the effect is well described by the model, both at 20–30 ns (blue) and 100–200 ns (orange). **d**, Here we plot the variation in the simulated magnetic field effect with B-field vector orientation within the (001) plane, since this parameter was unknown.

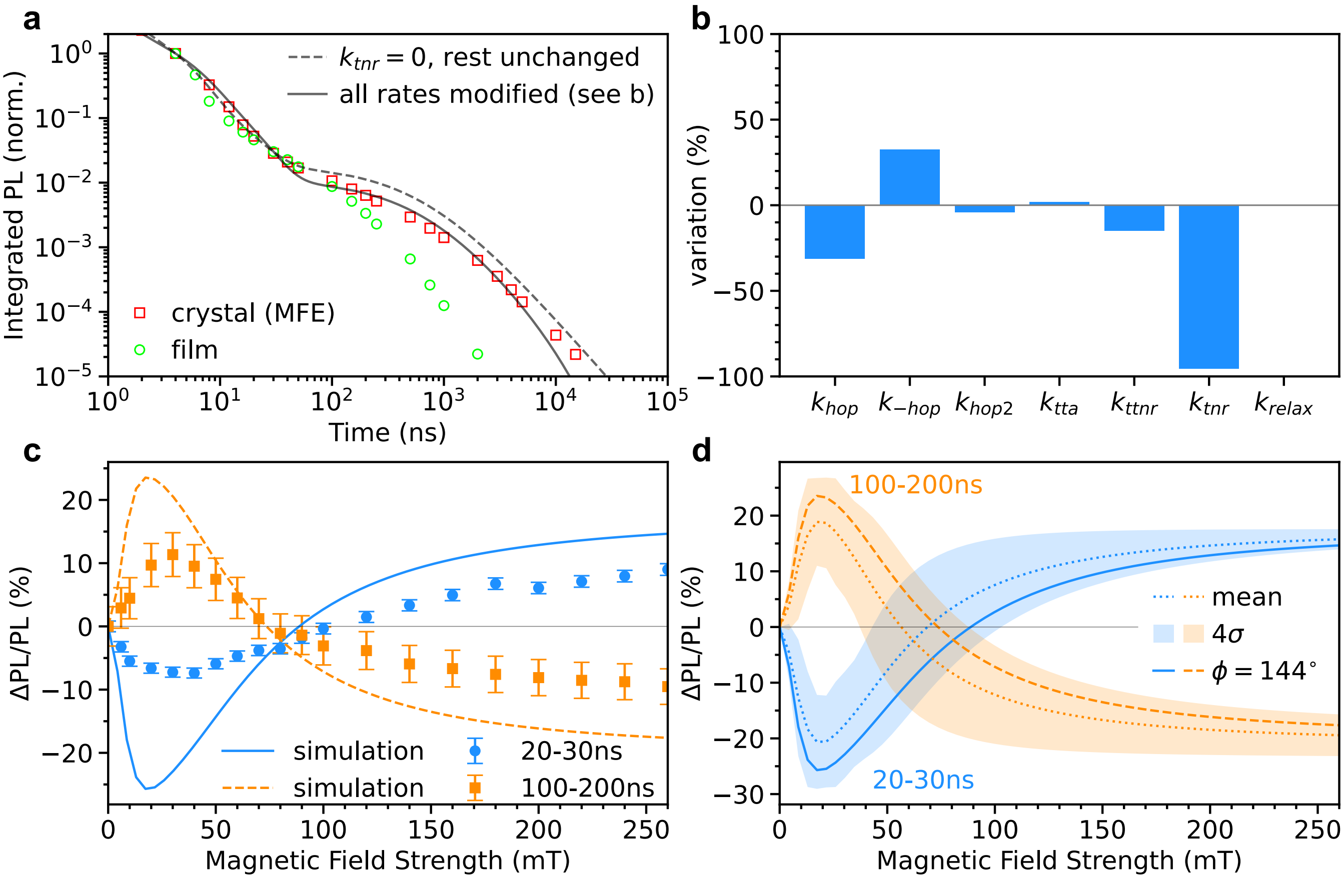

Figure 29 | Magnetic field effect on diftes single-crystal PL using the model presented in Section 6.6. **a**, Kinetics of the crystal (red) are longer lived than the film (green) beyond 100 ns. This is explained by an enhanced triplet lifetime (much smaller k_{tnr}) in the crystal. Using the same rate constants as for the film, but setting $k_{tnr} = 0$ (dashed line), we reproduce the crystal emission dynamics. For calculation of the magnetic field effect, rate constants were slightly optimised, yielding a better fit to the emission dynamics (solid line). **b**, Change in optimised rate constants compared to their initial (film) values. **c**, Measured (markers) and simulated (lines) magnetic field effect, using the model described in Section 6.6. Excepting the overall magnitude, the effect is well described by the model, both at 20–30 ns (blue) and 100–200 ns (orange). **d**, Here we plot the variation in the simulated magnetic field effect with B-field vector orientation within the (001) plane, since this parameter was unknown.

7.2.1 Considering separate S_1 and ^{1}(TT) states is important.

In Merrifield's model, ^{1}(TT) is not included. At room temperature, a significant proportion of the diftes emission arises from the S_1 state, which is anyway expected to be in equilibrium with ^{1}(TT) on the timescales of our measurements. We thus use Merrifield's kinetic scheme to obtain a description of the measured 'singlet' emission dynamics of our dropcast diftes crystal. As above, we fixed the values of k_{sf} and k_{snr} and set $k_{tnr} = 0$. This left 4 rate constants to be varied; namely k_{-sf}, k_{hop}, k_{tta} and k_{ttnr} (refer to equations 3-5). Figure 30a shows that a good fit to the data can be obtained. Figure 30b shows that whilst a good description of the magnetic field effect is obtained at 20–30 ns delay (blue), at 100–200 ns (orange) the model predicts almost no effect at all. This is because, as pointed out in the main text, the magnetic field dependence arises from ^{1}(TT) ↔ (T..T), which occurs on a longer timescale than singlet fission (S_1 ↔ ^{1}(TT)). Merrifield's model effectively combines these two distinct steps into one and as such fails to describe the time dependence of the magnetic field effect. We note that the steady-state magnetic field effect is likely to be well described by Merrifield's model, highlighting the importance of performing time-resolved measurements.

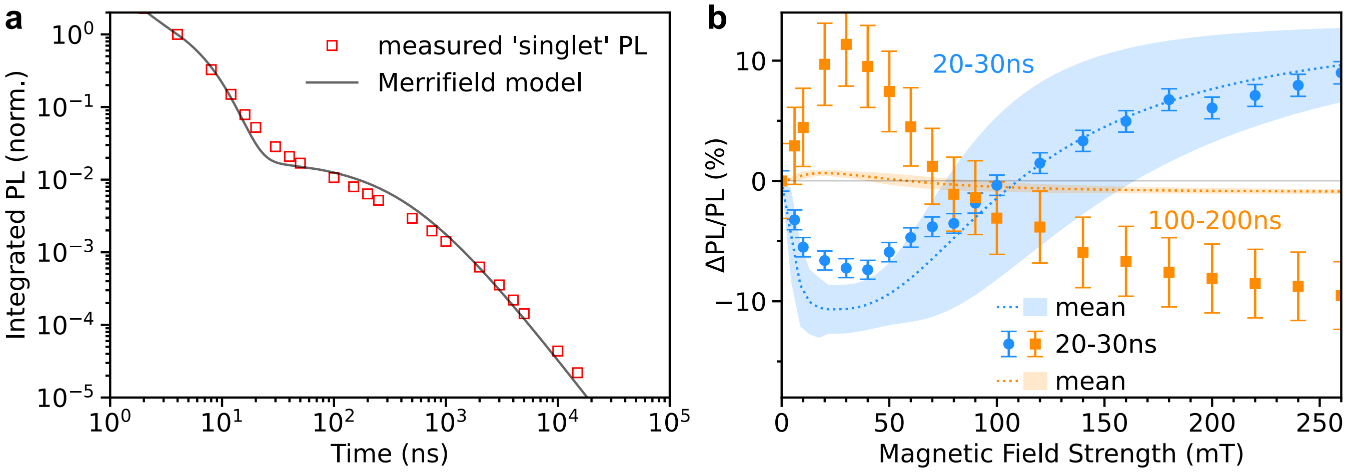

Figure 30 | Merrifield's model does not describe both kinetics and magnetic field effect. **a**, The singlet emission dynamics of the diftes crystal (red markers) can be well described by Merrifield's scheme. **b**, The magnetic field effect is very well described at 20–30 ns delay (blue), however the model predicts almost no effect at 100–200 ns (orange), in contrast to our measurement. The shading corresponds to the variation in the simulated magnetic field effect with B-field vector orientation within the (001) plane, since this parameter was unknown.

7.2.2 Further parameter variation to reproduce the magnitude of the MFE.

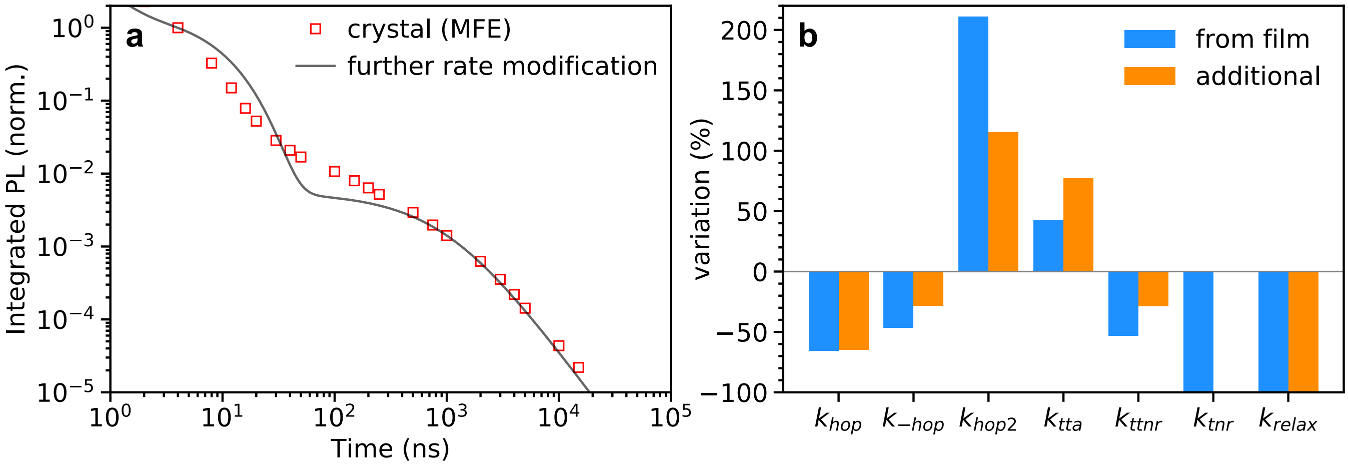

Figure 31 | Further rate constant variation. **a**, The reproduction of the PL kinetics is slightly poorer but the magnitude of the MFE is correct (see Figure 4c, main text). **b**, Variation of the rate constants with respect to the thin film (blue) and those in Figure 28 (orange).

Whilst the shape and time dependence were well reproduced by the initial modelling, the magnitude was overestimated by a factor of 2 (Figure 28c). We found that further small adjustments to the rate constants yielded an acceptable reproduction of the TRPL (Figure 31). We further varied the D and E parameters within the experimental errors given in Ref. 6 ($D : \pm 0.335\,\mu\text{eV}, E : \pm 0.125\,\mu\text{eV}$) to fine tune the zero crossing point of the MFE simulation. Finally, a relaxation of the constraint on the angle of the magnetic field with respect to the crystal enabled us to obtain a quantitative reproduction of the measured effect. This is presented in Figure 4c of the main text.

8 Excimers in diftes at 250 K and low excitation density.

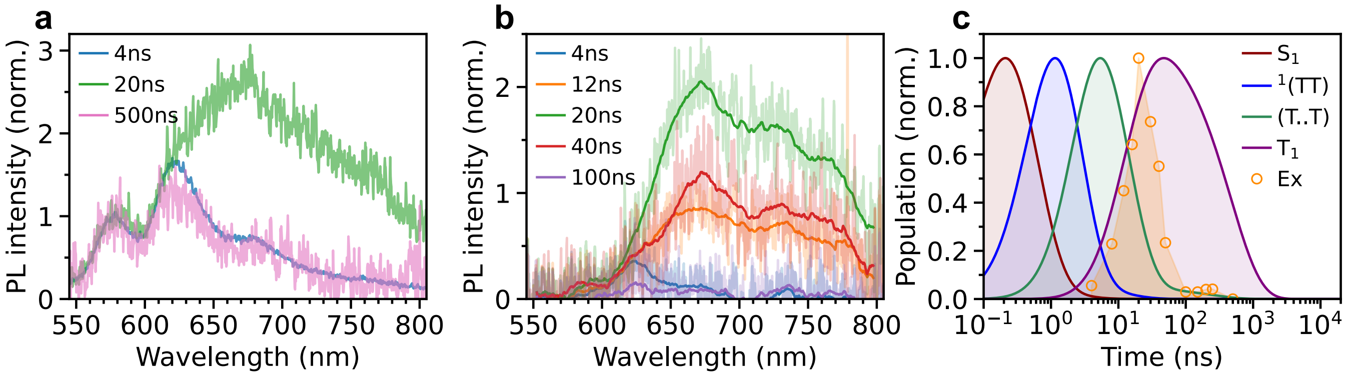

Figure 32 | Excimers in diftes at 100 K. **a**, Time-gated spectra of a diftes thin film at 250 K, 4, 20 and 500 ns after excitation with an initial excitation density of 10^{17}cm^{-3}. **b**, Subtraction of the 500 ns spectra (S_1 and ^{1}(TT) only) from the early-time data yields the excimer spectrum as a function of time. The integrated PL dynamics of the excimer are shown in **c**. **c**, Simulated population dynamics for diftes at 250 K and an initial excitation density of 10^{17}cm^{-3} using the kinetic model described in the text. The rise of the excimer PL (yellow markers) coincides with the rise of free triplets.

Figure 32a shows time-gated spectra of a diftes thin film at 4, 20 and 500 ns after excitation with an initial excitation density of 10^{17}cm^{-3}. Over the first 20 ns, a broad excimeric feature grows in which disappears by 100 ns, leaving only the S_1 and ^{1}(TT) spectra. To isolate the excimer component, we subtract the unchanging S_1 and ^{1}(TT) spectra at 500 ns from the early-time data. The excimer spectrum as a function of time delay is shown in Figure 32b and its dynamics are shown by the markers in Figure 32c, alongside excited state populations simulated using the kinetic model described in the main text and Section 6.3. Interestingly, the rise of the excimer emission appears to match the growth of the free triplet population.

We do not have enough data to determine with any kind of certainty the behaviour of excimers in this system since we only observed them under specific conditions (and not at all at 100 K which is the main focus of this paper). What follows is a very brief discussion of a few possible behaviours for the excimers, for interested readers.

It is perhaps surprising that the rise in the excimer population appears to occur so late, well after the decay of the singlet exciton. It could be that the excimers are indeed forming from singlet excitons at sites in the film more suited to excimer relaxation. Such a parallel pathway has been proposed for crystalline tetracene[31]. Alternatively, excimers may be forming from triplets, as has recently been shown in perylene[32].

9 Pentacene single crystal PL

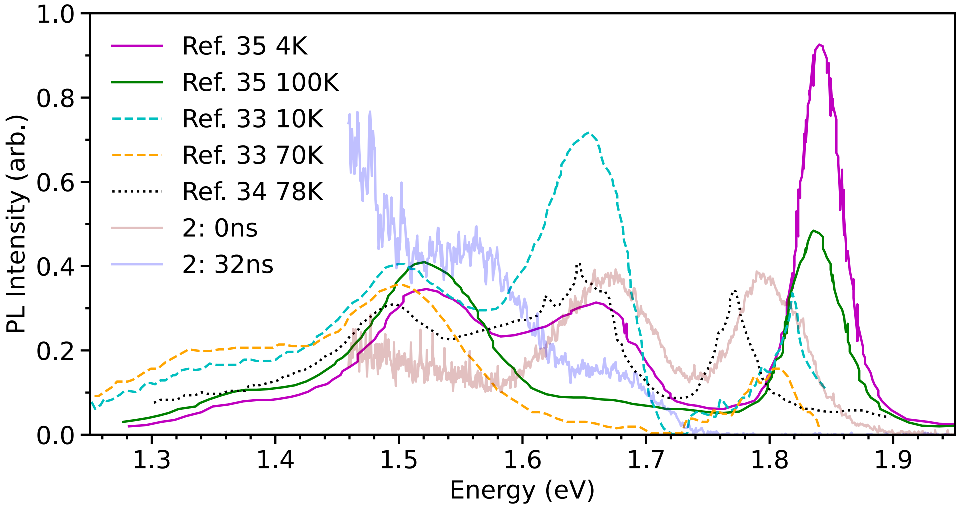

Figure 33 | Comparison of measured pentacene emission spectra. Our time-gated spectra (faint red and blue lines) are plotted against previously reported steady-state spectra from single crystals[33,34] and high-quality thin films[35]. All the features in our time-resolved data can be found in the literature spectra. Purple and green lines adapted from Reference 35, with the permission of AIP Publishing. Blue and orange dashed lines adapted from Reference 33 with the permission of World Scientific Publishing Co. Black dashed line adapted from Reference 34, with the permission of AIP Publishing.

Figure 33 shows a comparison of our time-gated spectra with literature steady-state spectra. There are small amounts of variation between the different measurements. Nevertheless, all show the same four emission bands at around 1.85 eV, 1.65 eV, 1.5 eV and 1.35 eV.

9.1 Raw data

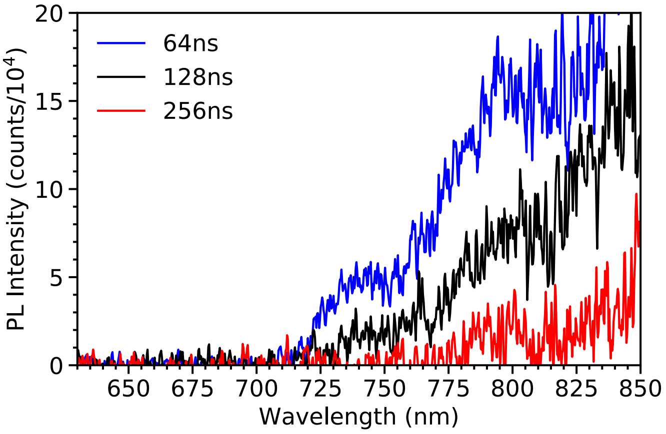

Figure 34 | Pentacene PL on long timescales. Spectra are shown for the last 3 data points in Figure 6d of the main text, which have the worst signal to noise ratio. The noise in these spectra is reflected in the error bars of Figure 6d, main text.

Figure 34 shows the raw data for the PL kinetics measured on pentacene single crystal **2** at the three longest delay times. These spectra, together with the error bars on the data presented in the main text, give a good idea of the fidelity of the dataset.

Figure 35 shows the raw data from which the fluence dependence reported in the main text was calculated. The signal to noise ratio at 750 nm is reasonably good for all fluences measured.

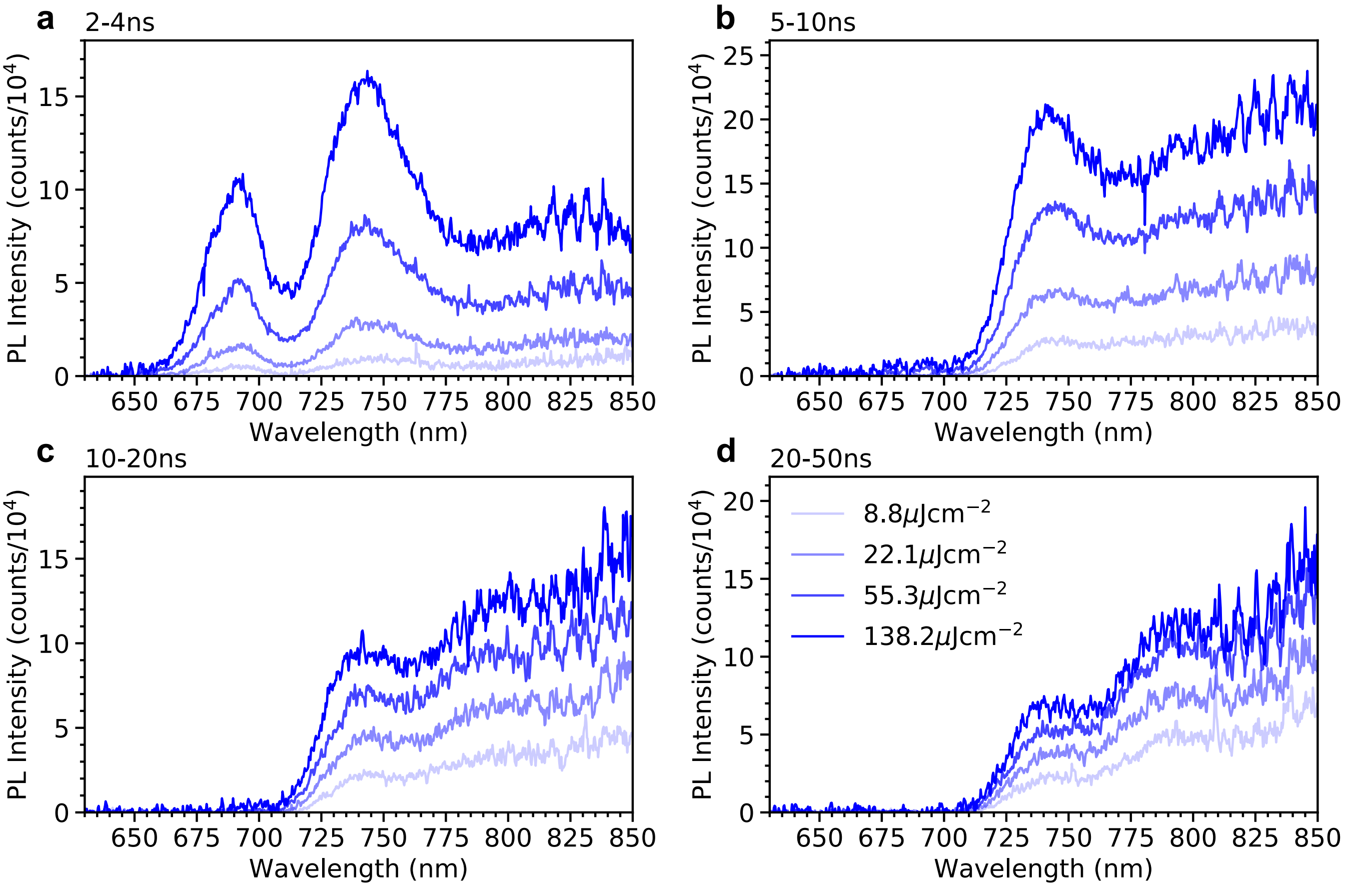

Figure 35 | Pentacene time-gated fluence dependence. PL spectra as a function of laser pulse energy at delay times of 2–4 ns (**a**), 5–10 ns (**b**), 10–20 ns (**c**) and 20–50 ns (**d**). The good signal to noise ratio of all the spectra is reflected in the small error bars of Figure 6e, main text.

References

[1] Hallani, R. K. *et al.* Structural and electronic properties of crystalline, isomerically pure anthradithiophene derivatives. *Adv. Funct. Mater.* **26**, 2341–2348 (2016).

[2] Kim, C.-H. *et al.* Decoupling the effects of self-assembled monolayers on gold, silver, and copper organic transistor contacts. *Adv. Mater. Interfaces* **2**, 1400384 (2015).

[3] Subramanian, S. *et al.* Chromophore fluorination enhances crystallization and stability of soluble anthradithiophene semiconductors. *J. Am. Chem. Soc.* **130**, 2706–2707 (2008).

[4] Campbell, R. B., Robertson, J. M. & Trotter, J. The crystal structure of hexacene, and a revision of the crystallographic data for tetracene and pentacene. *Acta Crystallogr.* **15**, 289–290 (1962).

[5] Spano, F. C. & Silva, C. H- and j-aggregate behavior in polymeric semiconductors. *Annu. Rev. Phys. Chem.* **65**, 477–500 (2014).

[6] Yong, C. K. *et al.* The entangled triplet pair state in acene and heteroacene materials. *Nat. Commun.* **8**, 15953 (2017).

[7] Jaumot, J., Gargallo, R., de Juan, A. & Tauler, R. A graphical user-friendly interface for mcr-als: a new tool for multivariate curve resolution in matlab. *Chemom. Intell. Lab. Syst.* **76**, 101–110 (2005).

[8] Johnson, R. C. & Merrifield, R. E. Effects of magnetic fields on the mutual annihilation of triplet excitons in anthracene crystals. *Phys. Rev. B* **1**, 896–902 (1970).

[9] Burdett, J. J., Piland, G. B. & Bardeen, C. J. Magnetic field effects and the role of spin states in singlet fission. *Chem. Phys. Lett.* **585**, 1–10 (2013).

[10] Tapping, P. C. & Huang, D. M. Comment on "magnetic field effects on singlet fission and fluorescence decay dynamics in amorphous rubrene". *J. Phys. Chem. C* **120**, 25151–25157 (2016).

[11] Scholes, G. D. Correlated pair states formed by singlet fission and exciton–exciton annihilation. *J. Phys. Chem. A* **119**, 12699–12705 (2015).

[12] Burdett, J. J. & Bardeen, C. J. Quantum beats in crystalline tetracene delayed fluorescence due to triplet pair coherences produced by direct singlet fission. *J. Am. Chem. Soc.* **134**, 8597–8607 (2012).

[13] Piland, G. B., Burdett, J. J., Kurunthu, D. & Bardeen, C. J. Magnetic field effects on singlet fission and fluorescence decay dynamics in amorphous rubrene. *J. Phys. Chem. C* **117**, 1224–1236 (2013).

[14] Wakasa, M. *et al.* What can be learned from magnetic field effects on singlet fission: Role of exchange interaction in excited triplet pairs. *J. Phys. Chem. C* **119**, 25840–25844 (2015).

[15] Yago, T., Ishikawa, K., Katoh, R. & Wakasa, M. Magnetic field effects on triplet pair generated by singlet fission in an organic crystal: Application of radical pair model to triplet pair. *J. Phys. Chem. C* **120**, 27858–27870 (2016).

[16] Ishikawa, K., Yago, T. & Wakasa, M. Exploring the structure of an exchange-coupled triplet pair generated by singlet fission in crystalline diphenylhexatriene: Anisotropic magnetic field effects on fluorescence in high fields. *J. Phys. Chem. C* **122**, 22264–22272 (2018).

[17] Pensack, R. D. *et al.* Observation of two triplet-pair intermediates in singlet exciton fission. *J. Phys. Chem. Lett.* **7**, 2370–2375 (2016).

[18] Stern, H. L. *et al.* Vibronically coherent ultrafast triplet-pair formation and subsequent thermally activated dissociation control efficient endothermic singlet fission. *Nat. Chem.* **9**, 1205 (2017).

[19] Trinh, M. T. *et al.* Distinct properties of the triplet pair state from singlet fission. *Sci. Adv.* **3**, e1700241 (2017).

[20] Chan, W.-L., Ligges, M. & Zhu, X.-Y. The energy barrier in singlet fission can be overcome through coherent coupling and entropic gain. *Nat. Chem.* **4**, 840–845 (2012).

[21] Bardeen, C. J. Time dependent correlations of entangled states with nondegenerate branches and possible experimental realization using singlet fission. *J. Chem. Phys.* **151**, 124503 (2019).

[22] Dover, C. B. *et al.* Endothermic singlet fission is hindered by excimer formation. *Nat. Chem.* **10**, 305–310 (2018).

[23] Singh-Rachford, T. N. & Castellano, F. N. Pd(ii) phthalocyanine-sensitized triplet-triplet annihilation from rubrene. *J. Phys. Chem. A* **112**, 3550–3556 (2008).

[24] Ogawa, T. *et al.* Donor–acceptor–collector ternary crystalline films for efficient solid-state photon upconversion. *J. Am. Chem. Soc.* **140**, 8788–8796 (2018).

[25] Gray, V., Moth-Poulsen, K., Albinsson, B. & Abrahamsson, M. Towards efficient solid-state triplet–triplet annihilation based photon upconversion: Supramolecular, macromolecular and self-assembled systems. *Coord. Chem. Rev.* **362**, 54–71 (2018).

[26] Lin, T.-A., Perkinson, C. F. & Baldo, M. A. Strategies for high-performance solid-state triplet–triplet-annihilation-based photon upconversion. *Adv. Mater.* **n/a**, 1908175 (2020).

[27] Wu, M. *et al.* Solid-state infrared-to-visible upconversion sensitized by colloidal nanocrystals. *Nat. Photonics* **10**, 31–34 (2016).

[28] Mongin, C., Garakyaraghi, S., Razgoniaeva, N., Zamkov, M. & Castellano, F. N. Direct observation of triplet energy transfer from semiconductor nanocrystals. *Science (80-.).* **351**, 369–372 (2016).

[29] Green, P. B., Li, Z. & Wilson, M. W. Pbs nanocrystals made with excess pbcl 2 have an intrinsic shell that reduces their stokes shift. *J. Phys. Chem. Lett.* **10**, 5897–5901 (2019).

[30] Nienhaus, L. *et al.* Speed limit for triplet-exciton transfer in solid-state pbs nanocrystal-sensitized photon upconversion. *ACS Nano* **11**, 7848–7857 (2017).

[31] Piland, G. B. & Bardeen, C. J. How morphology affects singlet fission in crystalline tetracene. *J. Phys. Chem. Lett.* **6**, 1841–1846 (2015).

[32] Ye, C., Gray, V., Mårtensson, J. & Börjesson, K. Annihilation versus excimer formation by the triplet pair in triplet–triplet annihilation photon upconversion. *J. Am. Chem. Soc.* **141**, 9578–9584 (2019).

[33] Aoki-Matsumoto, T. *et al.* Excitonic photoluminescence in pentacene single crystal. *Int. J. Mod. Phys. B* **15**, 3753–3756 (2001).

[34] He, R., Chi, X., Pinczuk, A., Lang, D. V. & Ramirez, A. P. Extrinsic optical recombination in pentacene single crystals: Evidence of gap states. *Appl. Phys. Lett.* **87**, 211117 (2005).

[35] Anger, F. *et al.* Photoluminescence spectroscopy of pure pentacene, perfluoropentacene, and mixed thin films. *J. Chem. Phys.* **136**, 054701 (2012).